

Developing theoretical and experimental tools for a hybrid quantum simulator based on trapped ions

by

Sainath Motlakunta

A thesis
presented to the University of Waterloo
in fulfillment of the
thesis requirement for the degree of
Master of Science
in
Physics (Quantum Information)

Waterloo, Ontario, Canada, 2018

© Sainath Motlakunta 2018

I hereby declare that I am the sole author of this thesis. This is a true copy of the thesis, including any required final revisions, as accepted by my examiners.

I understand that my thesis may be made electronically available to the public.

Abstract

Quantum simulation is the process of using a highly controllable quantum system to simulate another less controllable system. Quantum simulation can provide insights into the properties and dynamics of complex many-body systems. Trapped ion platform is one of the leading candidates for a quantum simulator due to its properties such as ease of isolation, preparation and manipulation. Simulating high dimensional spin systems enables us to study the various physical phenomena in higher geometries. Previous proposals for simulating higher dimensions require experimental resources that don't scale favourably with the system size[1]. In this thesis, we propose a hybrid (digital-analog) approach to simulate an effective 2D lattice from a 1D chain of trapped ions. In the initial geometry, the ions interact with each other through a flip-flop kind of interactions generated using a global Mølmer-Sørensen scheme [2, 3]. A series of single qubit gates are used to rescale and suppress the interactions in the initial chain to simulate the target geometry. These gates are applied using a laser field gradient which generates a site-dependent AC stark shift. I discuss the construction of this protocol in detail and the theoretical results for the case of 6, 9 and 16 ions. I also show that the number of gates and also the Stark gradient scale linearly with the system size.

Experimental implementation of an ion trap quantum simulator has various challenges, one of the which is the laser frequency stabilization within a fraction of transition linewidth. Traditionally, this is done by locking the lasers to an atomic transition. In this thesis, I discuss two alternative schemes for locking the laser frequencies used to build a $^{171}\text{Yb}^+$ ion quantum simulator. One of these solutions uses a commercial wavemeter as a measuring device for the frequency and feedbacks the lasers based on this measurement. I discuss the layout of this scheme and some results. Other solution uses a Fabry Perot (FP) cavity to transfer the stability of a stable laser to an unstable laser. In this thesis, I discuss the construction, optical layout and transmission measurements of a home-built FP cavity.

Acknowledgements

I am very grateful to my supervisor Dr. Kazi Rajibul Islam for giving me the opportunity to join this amazing research group (QITI Lab). I am thankful that he accepted me to transfer to QITI lab from my previous one, despite I had only 2 more terms left in my master's degree. I enjoy discussing physics with him and really appreciate his support during this period.

I want to thank my advisory committee members Dr. Crystal Senko and Dr. Michal Bajcsy for their valuable suggestions during the committee meetings. I enjoyed Dr. Senko's lectures on ion traps, which helped me a lot in transitioning into this new research area. I also thank Dr. Roger Melko for his valuable suggestions during my thesis defence.

I want to thank our collaborator Dr. Ashok Ajoy for motivating us to use the powerful tool of dynamical Hamiltonian engineering for the trapped ion platform and providing us with an initial sketch for this implementation.

I want to thank all my wonderful group mates Nikhil, Gilbert, Fereshteh, Nikolay, Roland and Yi Hong. It's been amazing working with our energetic theory postdoc Fereshteh, I have learnt a lot from this collaboration. I really enjoyed having discussions with students from Dr. Senko's group, Rich, Pei Jiang and Brendan.

I really appreciate the support from my previous lab mates Chang, Youn, Hyeran, Mahmood, Vinay, Somendu, Ying, Ashwin, Shengqiao and Leo. I also want to thank my friends Utkarsh, Haibo and Prathamesh who were a great support during this time.

Saying thanks would be something less, I feel privileged from the support I got from my parents and sister, whose blessings I always had.

Dedication

This thesis is dedicated to the efforts of generations of physicists.

Table of Contents

List of Tables	viii
List of Figures	ix
1 Introduction	1
1.1 Outline	4
2 Introduction to trapped ion platform	5
2.1 Interactions mediated in a chain of ions	8
3 Engineering 2D lattices in a 1D chain of ions	11
3.1 Hamiltonian setup	12
3.2 Case of 2 ions	13
3.3 Average Hamiltonian of a pulse sequence	14
3.4 Stark shift pattern to simulate 2D lattices	16
3.5 Construction of pulse sequence	17
3.6 Analysis and Results for 6 ions	19
3.6.1 Simulation with experimental parameters	24
3.7 Results for 9,16 ions	25
3.8 Scaling with the number of ions	27
3.9 Extension to 3D lattices	27
3.10 Discussion	28

4	Laser frequency stabilization	29
4.1	Wavemeter based frequency lock	30
4.2	Cavity based frequency lock	34
4.2.1	Cavity design	35
4.2.2	Cavity construction	36
4.2.3	Optical setup and cavity mode matching	38
4.3	Cavity transmission measurements	39
4.4	Optical layout for cavity based frequency lock	40
4.5	Discussion	41
5	Summary and Outlook	42
5.1	Engineering 2D lattices from 1D chain of ions	42
5.2	Laser frequency stabilization	43
	References	44
	List of Publications	46

List of Tables

3.1	Fourier series fit parameters for 6 ions	21
3.2	Pulse sequence parameters for 6 ions	21
3.3	Fourier series fit parameters for 9 ions	25
3.4	Fourier series fit parameters for 16 ions	26
4.1	Cavity mode matching parameters	39

List of Figures

1.1	Equivalence of a chain of ions and a fully connected graph	2
1.2	Types of quantum simulations	3
1.3	A 2D lattice of 16 ions	3
2.1	Chain of ions trapped in a Paul trap	5
2.2	Normal motional modes - 9 ions	6
2.3	$^{171}\text{Yb}^+$ energy level diagram	7
2.4	Raman lasers configuration	8
2.5	Raman lasers configuration for Mølmer-Sørensen scheme	8
2.6	Dependence of interaction profiles with the detuning μ	9
3.1	Transforming a fully connected geometry of 4 ions to a (2x2) square lattice	11
3.2	A chain of two ions.	13
3.3	Time evolution of the flip-flop Hamiltonian for 2 ions	13
3.4	Time evolution for 2 ions with an engineered interaction profile	13
3.5	General pulse sequence	14
3.6	Pulse sequence with Stark pulses interleaved with Hamiltonian inversion.	15
3.7	(2x2) geometry of 4 ions	16
3.8	Stark gradient scheme to simulate $m \times m'$ 2D lattice	16
3.9	A single cycle of the pulse sequence	18
3.10	Transformation of 6 ion fully connected system to a 3x2 square lattice	20

3.11 Stark gradient for 6 ions	20
3.12 6 ions - Fourier series fit	21
3.13 Pulse sequence for 6 ions	21
3.14 Time evolution plots for the case of 6 ions	22
3.15 6 ions pairwise time evolution plots	23
3.16 Hamiltonian estimation for the case of 6 ions	23
3.17 Hamiltonian estimation with experimental parameters for 6 ions	24
3.18 Stark gradient pattern for 9 ions	25
3.19 Hamiltonian estimation for the case of 9 ions	26
3.20 Stark gradient for 16 ions	26
3.21 Hamiltonian estimation for the case of 16 ions	27
3.22 Scaling of number of pulses	27
3.23 Transformation of a fully connected 8 ion chain to a (2x2x2) 3D lattice	28
3.24 Hamiltonian estimation for the case of 8 ions	28
4.1 Working of wavemeter	30
4.2 Drift of frequency due to ambient fluctuations	31
4.3 Wavemeter lock scheme	32
4.4 Response of the feedback circuit with the scanning of laser piezo	33
4.5 Locked laser vs unlocked laser	33
4.6 Cavity lock working	34
4.7 Predicted trasmission profile of the HR mirrors	35
4.8 Construction of cavity supports	36
4.9 Cavity vacuum enclosure	37
4.10 Fundamental mode of the cavity at 369nm	38
4.11 Mode matching for 369nm laser beam	39
4.12 Cavity transmission	40
4.13 Cavity lock optical layout	41

Chapter 1

Introduction

Understanding and predicting the properties as well as dynamics of complex physical systems have been one of the quests of generations of physicists. One of the heuristics to solve this class of problems is the bottom-up approach. We first try to identify, understand and postulate the fundamental building blocks that we guess would be the reasons for the target phenomenon. Modern fundamental theories like quantum mechanics, general relativity are the results of this approach. The next step in this bottom-up approach is using these postulates to predict and understand the properties by simulating or emulating complex physical systems. Traditionally mathematical and in the past century, computational (classical) tools have been used to perform this kind of simulations. However, this approach might not work for problems that require exponentially scaling resources with the system size.

In recent decades it has been realized that simulating many complex quantum mechanical systems with the bottom-up approach using the traditional tools is not practically feasible. Due to the properties like entanglement and quantum superposition, it requires an exponential amount of classical resources such as processing power on a computer, to simulate the dynamics of quantum mechanical systems. One solution to this problem as proposed by Feynman [4], is to use a highly controllable quantum mechanical system as our simulation tool. Various criteria needs to be satisfied by a system to be a candidate for a quantum simulator [5]. These criteria for quantum simulation can be achieved in several physical systems, such as trapped ions, NMR, superconducting qubits, ultracold atoms, NV center diamonds etc.,

The trapped ion platform is one of the leading candidates for quantum simulation because of the properties such as ease of preparation, isolation and control, with near

perfect state initialization and detection. Long coherence times as high as few minutes have been reported [6] for the case of $^{171}\text{Yb}^+$ ions. One of the most attractive features of trapped ions is the fully connected nature of their phonon mediated spin-spin interactions. Here, two hyperfine levels in each of the $^{171}\text{Yb}^+$ ions serve as the spin-1/2 systems. Though in a typical experimental realization, the geometry of the trapped ions is in the form of a linear chain, the phononic bus mediating the 2-body long-range interactions make it a fully connected system. Fig. 1.1 shows a chain of 5 ions (blue circles) trapped in a Paul trap, the red lines between them represent the coupling strengths. This system of linear chain of ions is equivalent to a fully connected graph of interactions, as shown at the right of the figure.

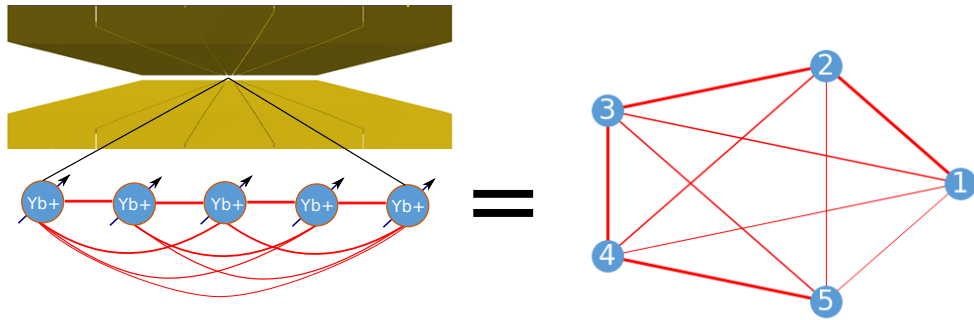


Figure 1.1: Equivalence of a chain of ions and a fully connected graph

A typical quantum simulation experiment using trapped ions starts by initializing the quantum system to a known state, then evolving the state under the simulated Hamiltonian which is followed by a set of measurements. The simulations can be broadly classified into two categories, analog and digital, based on the procedure of emulating the Hamiltonian. In an analog quantum simulation, the Hamiltonian of the simulator is modified to match the target Hamiltonian, whereas in a digital simulation the target Hamiltonian is decomposed into a series of single and two qubit gates that are sequentially applied on the initial state to reach the final state. Though the digital simulation is more universal, errors due to this digitization build up as the system size increases. On the other hand, analog simulations are not prone to digitization errors, but can only simulate a restricted set of Hamiltonians.

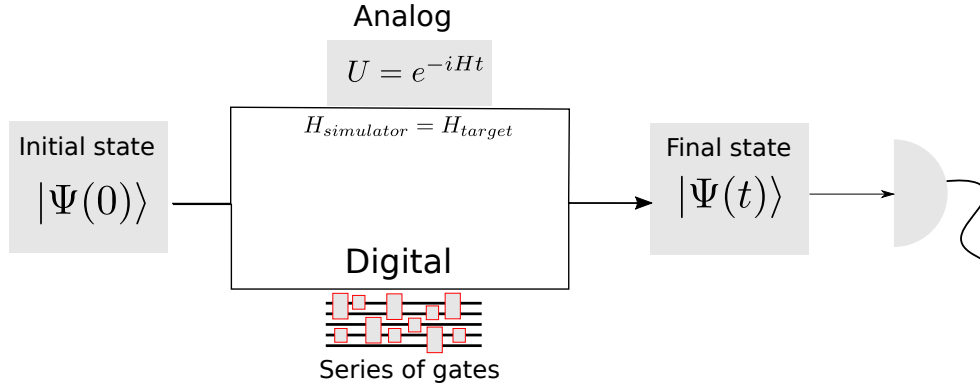


Figure 1.2: Types of quantum simulations

In this thesis, we investigate a hybrid analog-digital scheme to simulate a Hamiltonian that is not easily obtained in the system of a chain of trapped ions. We would like to simulate a 2D spin model on a square lattice in a 1D chain of trapped ions. Simulating high dimensional spin systems enables us to study the various physical phenomena in higher geometries. Fig. 1.3 shows a graph where the nodes are Yb+ ions and the edges represent non-zero interaction between the ions. This arrangement of interactions transforms a linear chain of 16 ions to an effective 4x4 2D lattice geometry. To simulate this geometry from a linear ion chain using an analog quantum simulation requires arbitrarily programmable intensity and frequency controls at the level of individual ions [1]. This approach is not favourably scalable with the system size. Whereas, for a case of digital simulation, errors accumulate from single and two qubit gates for large systems. To overcome these problems, in this thesis, we propose a hybrid (analog-digital) simulation scheme (Chapter 3) to generate an effective 2D lattice. This is done by modulating the spin-spin interactions [7] using a global laser gradient field. This hybrid simulation scheme requires less experimental controls than a fully analog or fully digital scheme to solve the same problem.

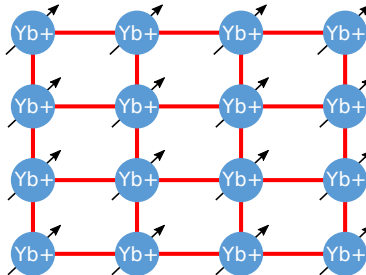


Figure 1.3: A 2D lattice of 16 ions

Experimental implementation of this approach to simulate large quantum systems using trapped ions has various steps of trapping, preparing, manipulating and detecting the spin states. This requires setting up highly sensitive ultra-high vacuum chambers, frequency-stabilized lasers and other experimental tools involving digital, analog and RF electronics. There are various challenges in setting up these tools. One such challenge is to frequency stabilize the lasers to an atomic transition. The traditional ways of stabilizing the lasers against ambient drifts use atoms as references. In this thesis, I discuss the implementation of two alternative schemes to frequency stabilize the lasers.(chapter 4).

1.1 Outline

The following is the brief outline of this thesis

- Chapter 2 discusses some fundamentals aspects of trapped ions platform which one would need to understand the implementation of our scheme for hybrid quantum simulation.
- Chapter 3 describes the intuition, protocol construction and some results for engineering 2D lattices from 1D chain of trapped ions.
- Chapter 4 describes the scheme, construction and some results for frequency locking the lasers against the ambient drifts in the context of our lab.
- Chapter 5 concludes the thesis with a brief note on the future outlook.

Chapter 2

Introduction to trapped ion platform

In this chapter, I will briefly describe the trapped ion platform and some of the theoretical tools one needs to understand to implement the hybrid (analog-digital) quantum simulations described in chapter. 3.

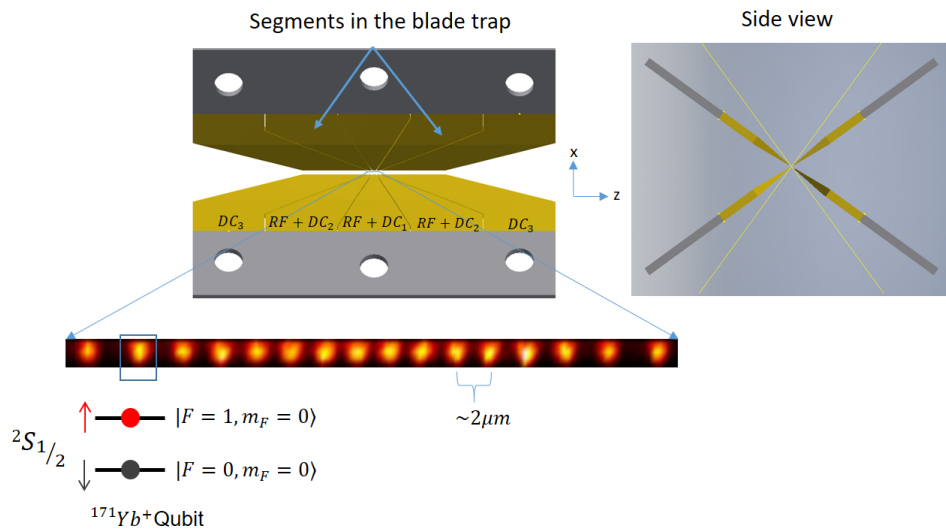


Figure 2.1: Chain of ions trapped in a Paul trap. CCD image taken from [8]

In the context of our experiments, two hyperfine levels of ground state of $^{171}\text{Yb}^+$ ion are used as $|\uparrow\rangle$ and $|\downarrow\rangle$ spin states. In order to perform quantum simulation experiments using these ions, one must be able to create, isolate and manipulate a collection of ions,

induce interactions between spins. To trap a chain of ions, a beam of neutral Yb atoms is ionized using a pair of lasers which are tuned to kick out the valence electron. The ionised Yb atoms are then trapped using electric fields. As a charged particle cannot be held in space using just electrostatic field because local extrema cannot exist in an electrostatic potential (Earnshaw’s theorem). One of the solutions to circumvent this problem is to use oscillating electric fields in addition to electrostatic fields. Thus creating an effective extremum in the time average potential. A combination of electrodes is used to apply these fields to trap the ions at the potential minimum. One such arrangement of electrodes we are trying to implement in our lab is a blade trap Fig. 2.1. In this geometry, 4 segmented blades are arranged to form a cross, trapping a chain of ions at the center.

This geometry creates a 3D confining potential with effective trap frequencies $\omega_X, \omega_Y, \omega_Z$. The dimensions of the geometry are chosen such that the resulting trap frequencies are higher in X and Y directions when compared to that of the Z ($\omega_X \approx \omega_Y \gg \omega_Z$). When ions are trapped in this trap, the attracting force due to the confining potential and the coulombic repulsive potential act against each other. This leads to an equilibrium position of a linear chain of ions. This chain of ions oscillate around the equilibrium positions on perturbation. These oscillations can be decomposed into eigen normal modes of motion in X,Y,Z directions. The normal modes in X,Y direction (transverse modes) are typically designed to have higher frequencies than that of the Z direction (axial modes). Fig. 2.2, show the frequencies and eigen mode vectors of transverse oscillations for a chain of 9 ions. Here we chose $\omega_X = 2\pi \times 5$ MHz and $\omega_Z = 2\pi \times 1$ MHz. The normal mode of highest frequency is called the Center of Mass (COM) mode where the eigenvector amplitudes are equal for all the ions. The next highest frequency is the tilt mode where ions at the end of the chain have higher amplitudes of oscillation.

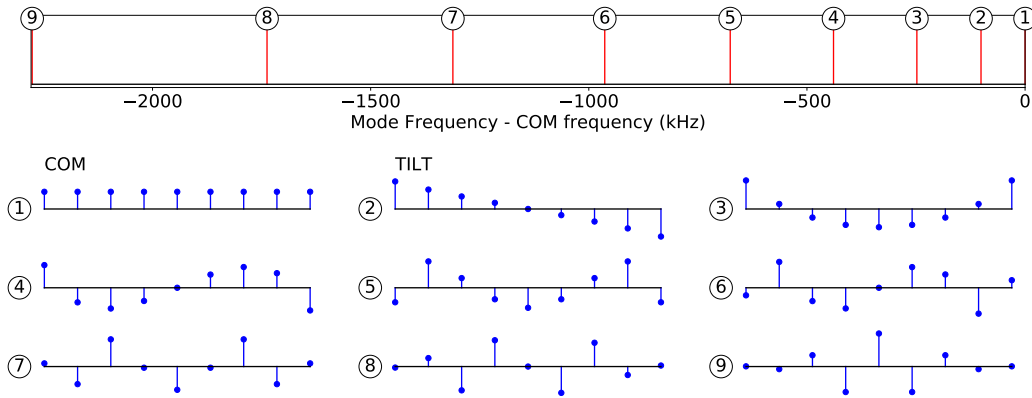


Figure 2.2: Normal motional modes - 9 ions

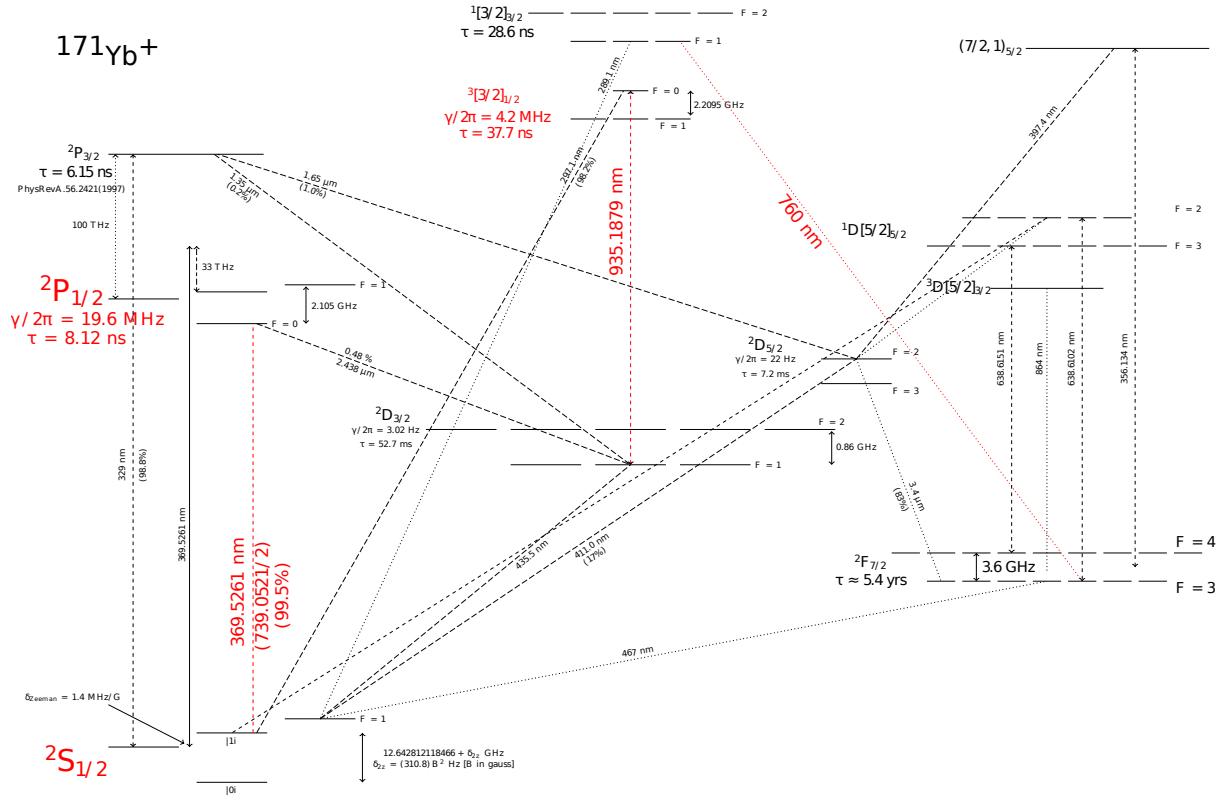


Figure 2.3: $^{171}\text{Yb}^+$ energy level diagram

Once a chain of ions is trapped, they need to be initialized to motional and spin ground states to perform the quantum simulation experiments. This is done by using a combination of laser beams performing laser cooling, sideband cooling, optical pumping and repumping of the ions to the ground state. Lasers with wavelengths 369nm, 760nm and 935nm are used to perform these operations. Here cooling and optical pumping require the generation of sidebands using an Electro-Optic modulator (EOM) at 14.7 GHz and 2.1 GHz respectively [9]. The energy level scheme of $^{171}\text{Yb}^+$ ions featuring various transition wavelengths is shown in Fig. 2.3. As we can notice that the linewidths of these transitions are in the order of few MHz, the lasers need to be tuned and stabilized to these wavelengths continuously to deterministically perform the quantum simulations experiments. Locking schemes to perform this task are discussed in more detail in chapter 4.

2.1 Interactions mediated in a chain of ions

In this section, we briefly describe the mechanism for engineering an XY or flip-flop spin-spin interactions. This Hamiltonian will be used for simulations discussed in Chapter 3. In a chain of ions, we use vibrational phonons of the chain to mediate interactions between ions. This is done using Mølmer-Sørensen interaction scheme [2] which uses a combination of lasers that induce off-resonant Raman transitions between the spin and vibrational states of the ions. To briefly understand this scheme, consider a pair of counter propagating Raman lasers with frequencies ν_1 and ν_2 incident on a chain of ions (Fig. 2.4). These lasers are tuned such that the beatnote produced due to difference in frequencies, can excite transitions between spin-phonon states. (Fig. 2.4). Two such off-resonant beat notes with frequencies $\nu_{qubit} + \mu$ and $\nu_{qubit} - \mu$ (Fig. 2.5) induce an effective Ising interactions between spins (coupling $\downarrow\downarrow$ with $\uparrow\uparrow$ and $\downarrow\uparrow$ with $\uparrow\downarrow$).

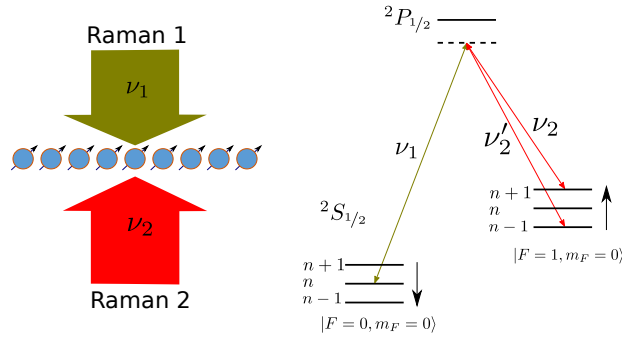


Figure 2.4: Raman lasers configuration

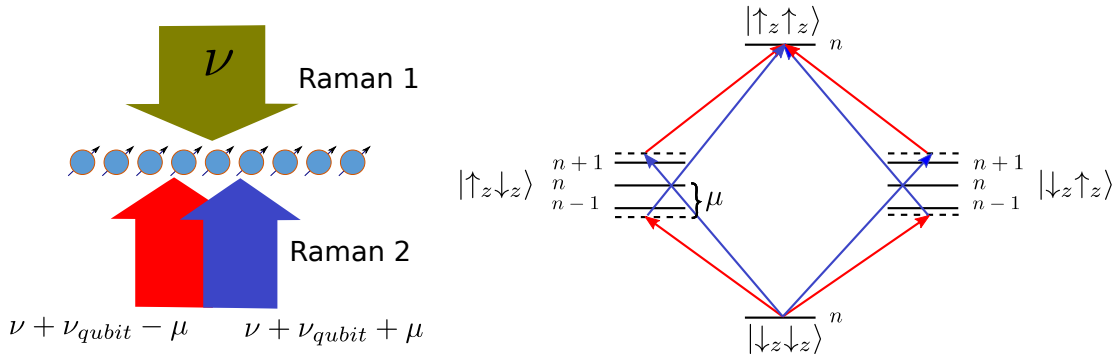


Figure 2.5: Raman lasers configuration for Mølmer-Sørensen scheme

This Molmer-Sorensen scheme induces an effective $S_i^x S_j^x$ type interaction between every pair of ions (i, j) with a coupling strength J_{ij} .

$$H_{eff} = H_{XX} = \sum_{i>j} J_{i,j} S_i^x S_j^x \quad (2.1)$$

$$J_{i,j} = \Omega_i \Omega_j \left(\frac{\hbar \Delta k^2}{2m} \right) \sum_k \frac{b_i^k b_j^k}{\mu^2 - \omega_k^2} \quad (2.2)$$

Here the sum (k) is over all the vibrational normal modes of the chain (Fig. 2.2), b_j^k is the eigen vector component of ion j for the vibrational mode k , ω_k is the frequency of the normal mode. Ω_i is the Rabi frequency of the lasers on ion i and μ is the detuning from the carrier transition. From the eqn. 2.2 we can see that the value of μ decides the profile of J_{ij} . Fig. 2.6 summarizes the dependency of μ . If μ is chosen close the COM mode, since the eigen vector amplitudes are same for all the ions, the scheme produces an interaction profile with nearly equal interaction strength. Whereas if it is chosen close to the tilt mode, the resulting interaction profile increases with ion distance. Thus various interaction profiles can be generated by just changing the detuning, though the inverse problem of finding the detuning and Rabi frequency, given an interaction profile is not trivial. A hybrid approach to solve this inversion problem is discussed in chapter 3.

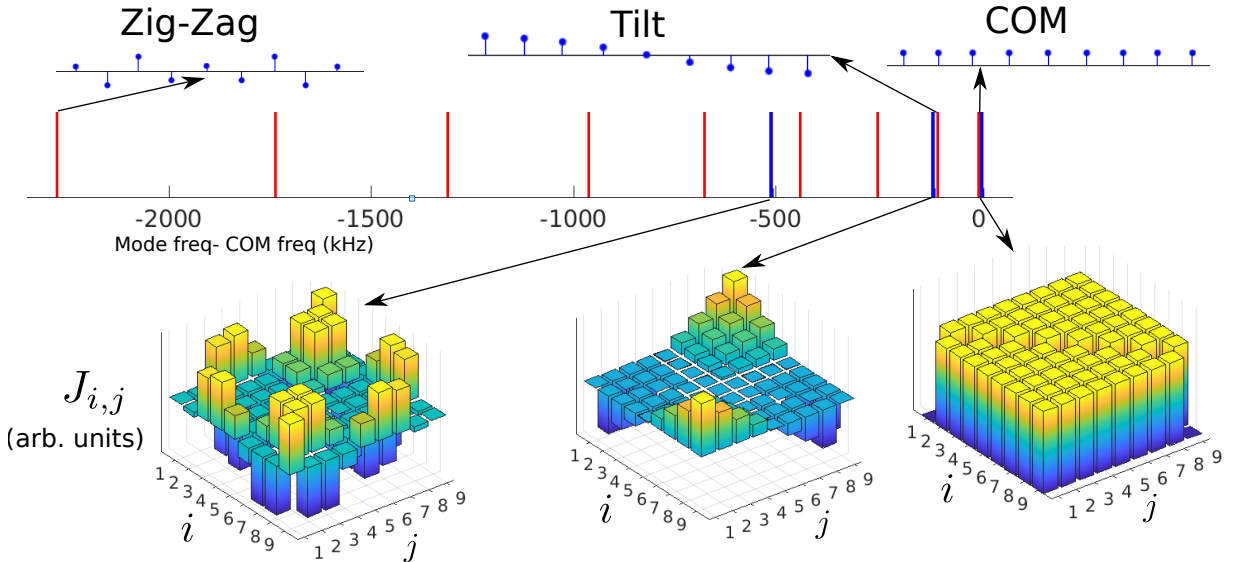


Figure 2.6: Dependence of interaction profiles with the detuning μ , for the case of 9 ions trapped in a harmonic trap with trap frequencies $\omega_x=5$ MHz, $\omega_z=1$ MHz

Using this protocol to produce Ising interactions of type $S_i^x S_j^x$ and by adding an additional bias field, the coupling created between $|\downarrow\downarrow\rangle$ and $|\uparrow\uparrow\rangle$ can be eliminated, retaining only the couplings between $|\downarrow\uparrow\rangle$ and $|\uparrow\downarrow\rangle$. Thus simulating flip-flop $S_i^+ S_j^-$ kind of interactions (H_{XY}) [3] under the condition that $|B_z| \gg |J_0|$

$$H_{XX} + B_z \sum_i S_i^z \xrightarrow{|B_z| \gg |J_{i,j}|} H_{XY}$$

where

$$H_{XY} = \sum_{i < j} J_{ij} S_i^+ S_j^- + h.c.$$

In Chapter 3, we present a protocol to engineer a target interaction profile J_{ij} . We will present solutions for effectively creating a 2D spin lattice in a 1D chain of ions, by suitably manipulating the interaction graph.

Chapter 3

Engineering 2D lattices in a 1D chain of ions

In this chapter I will be describing the theoretical framework and some results of simulating a two dimensional square lattice from a one dimensional chain of trapped ions. Before going into further details, let me first briefly explain the idea behind this scheme. This scheme of hybrid (analog-digital) quantum simulation relies on digitally modulating an analog quantum simulation

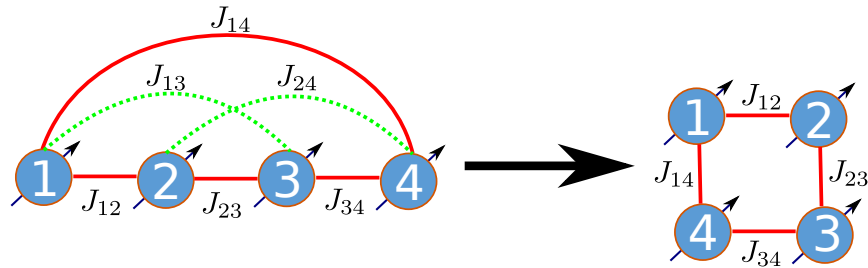


Figure 3.1: Transforming a fully connected geometry of 4 ions to a (2x2) square lattice

1. **Analog:** For a given 1D chain of ions, we first create an interaction profile between ions that is simulated using a global Mølmer-Sørensen scheme as described in [2] Chapter 2. For example, in the case of 4 ions, to simulate a 2x2 lattice, we start by simulating a fully connected geometry with equal interactions by choosing a global Mølmer-Sørensen detuning close to the COM mode.

2. **Digital:** We then suppress and rescale some of the unwanted spin interactions by applying a series of single spin operations. In case of 4 ions, to simulate a square lattice starting from a fully connected geometry, this protocol suppresses J_{13} and J_{24} (Fig.3.1) In our scheme these single spin operations are applied via laser induced site dependent AC Stark shift.

In the following sections, I will describe in detail the digital part of our scheme.

3.1 Hamiltonian setup

Consider a linear chain of n ions, we assume that every pair of ions (i, j) interact with each other via a flip-flop ($S_i^+ S_j^-$) kind of interaction with a coupling strength of J_{ij} . We assume an initial long range interaction profile of form $J_{ij} = \frac{J_0}{|i-j|^\alpha}$ where $\alpha \in (0, 3)$ and J_0 is a scaling factor. Thus the initial Hamiltonian H_{XY} can be written as

$$H_{XY} = \sum_{i < j} J_{ij} S_i^+ S_j^- + h.c. \quad (3.1)$$

Such a Hamiltonian can be generated starting from an XX Hamiltonian by applying a large effective magnetic field along the Z-axis as described in Chapter 2. To achieve the goal stated in step 2 i.e to suppress or rescale the spin interactions in an initial spin graph, we require a way to distinguish these interactions. An ingredient to distinguish the interactions between various spins is a site dependent effective magnetic field ω_i . This field can be generated in an experiment by applying a laser beam with an inhomogeneous intensity profile, imparting a site dependent light (AC Stark) shift on the spins. This introduces an additional Hamiltonian (H_z) given as

$$H_{stark} = H_z = \sum_{i=1}^N \omega_i S_i^z$$

Under the action of H_z for a time τ , a pair of ions (i, j) in a state $|\psi_{ij}\rangle$ is transformed to a state $e^{i\omega_{ij}\tau} |\psi_{ij}\rangle$ where $\omega_{ij} = \omega_i - \omega_j$. Thus for a given time τ every pair of ions (i, j) acquires a phase of $\phi = \omega_{ij} * \tau$. This relative Stark shift ω_{ij} is used as a tag in our scheme to target the interactions.

3.2 Case of 2 ions

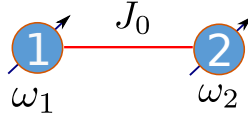


Figure 3.2: A chain of two ions.

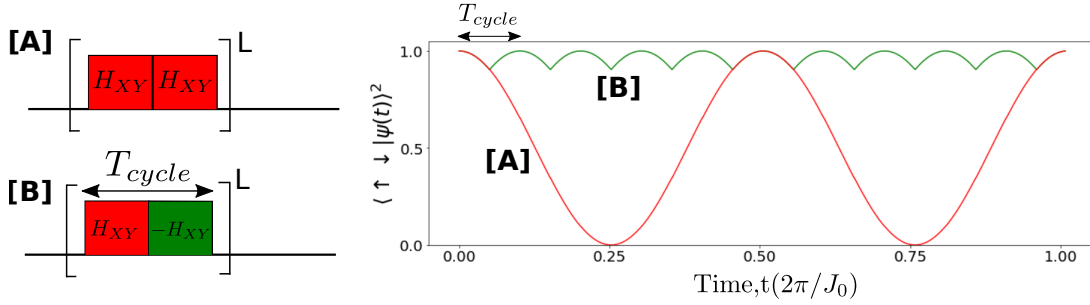


Figure 3.3: Time evolution of the flip-flop Hamiltonian for 2 ions

To understand how the spatially inhomogeneous field can effectively modify an XY interaction, consider a simple case of two ions interacting with a flip-flop Hamiltonian with a coupling strength J_0 . With an initial two qubit state $|\uparrow\downarrow\rangle$, the evolution of the state $|\psi_{12}\rangle$ under the flip-flop Hamiltonian oscillates between $|\uparrow\downarrow\rangle$ and $|\downarrow\uparrow\rangle$. This can be seen as trace [A] in Fig. 3.3 which shows $\langle\uparrow\downarrow|\psi_{12}(t)\rangle^2$ as a function of time. However, if the H_{XY} is reversed ($-H_{XY}$) after a time t , the evolution is inverted which is equivalent to time reversal evolution. If this inversion is done at regular intervals of time, the evolution is altered and the two qubit state is frozen(trace [B] in Fig. 3.4), This is equivalent to suppressing the interaction between the spins.

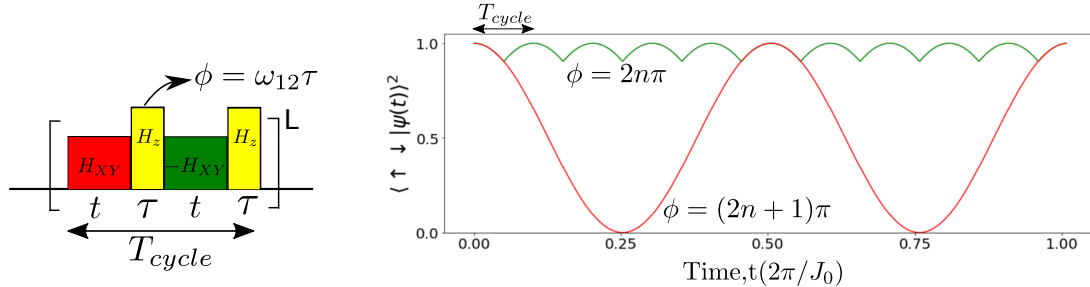


Figure 3.4: Time evolution for 2 ions with an engineered interaction profile

Now consider a sequence where an additional laser beam imprinting a site dependent Stark shift H_z is introduced in between the pulses of H_{XY} and $-H_{XY}$. Let ω_1 and ω_2 be the Stark shifts for the ions 1,2 respectively. This Stark shift introduces a relative phase of $\phi = \omega_{ij} * \tau$ where τ is the duration of the pulse. If we choose τ such that $\phi = (2n+1)\pi$, this changes the state $|\psi\rangle \rightarrow -|\psi\rangle$ thus cancelling the effect of the Hamiltonian inversion (Fig. 3.4). However, $\phi = 2n\pi$ retains the effect of Hamiltonian inversion. Thus by choosing τ such that

$$\begin{aligned}\phi = \omega_{ij} * \tau &= 2n\pi \rightarrow \text{Suppresses the interaction} \\ &= (2n+1)\pi \rightarrow \text{Retains the interaction}\end{aligned}$$

3.3 Average Hamiltonian of a pulse sequence

To utilize above mentioned scheme of suppressing the interactions for a case of an n ion network, we need to consider a more general pulse sequence scheme with multiple Stark pulses of different pulse widths interleaved with Hamiltonian inversion (Fig.3.5). The pulse widths have to be optimized to get the desired interaction graph. This requires an understanding of the effective Hamiltonian of this pulse sequence. In this section, I will be describing the average Hamiltonian for such an arbitrary pulse sequence.

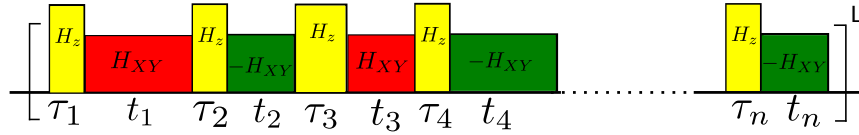


Figure 3.5: General pulse sequence

Consider a 1D chain of n ions interacting via H_{XY} . An additional laser induces a site dependent AC Stark shift ω_i introducing additional Hamiltonian H_Z . In presence of both H_{XY} and H_z , with $\omega_i \gg J_0$ we can consider the effective Hamiltonian in interaction picture as

$$\tilde{H}_{eff} = e^{-iH_Z\tau} H_{XY} e^{iH_Z\tau} = \sum_{i>j} J_{i,j} S_i^+ S_j^- e^{i\omega_{ij}\tau} + h.c$$

But for a pulse sequence with Stark pulses interleaved with Hamiltonian inversion, the effective Hamiltonian can be approximated by an average Hamiltonian.

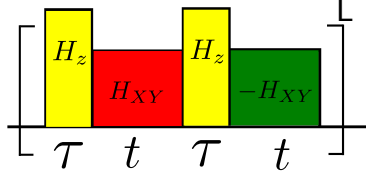


Figure 3.6: Pulse sequence with Stark pulses interleaved with Hamiltonian inversion.

For a single cycle of a pulse sequence shown in Fig. 3.6,

$$H_{avg} = \sum_{i>j} J_{i,j} S_i^+ S_j^- (e^{i\omega_{ij}\tau} - e^{2i\omega_{ij}\tau}) + h.c$$

for L cycles

$$H_{avg} = \sum_{i>j} J'_{i,j} S_i^+ S_j^- + h.c$$

where

$$J'_{i,j} = \frac{J_{ij}}{L} * (e^{i\omega_{ij}\tau_{tot}} - e^{2i\omega_{ij}\tau_{tot}} + \dots e^{Li\omega_{ij}\tau_{tot}}) \quad (3.2)$$

Thus we obtain a flip-flop Hamiltonian whose interaction strength is transformed to J'_{ij} . We can see that if we choose $\omega_{ij} * \tau_{tot} = 2n\pi$, $J'_{i,j} = 0$ thus suppressing the interaction between ion i and ion j . But for a more general pulse sequence of form Fig. 3.5, the average Hamiltonian for one cycle would be

$$H_{avg} = \sum_{i>j} J''_{i,j} S_i^+ S_j^- + h.c \quad (3.3)$$

with

$$J''_{i,j} = \frac{J'_{i,j}}{T_{cycle}} * (t_1 e^{i\omega_{ij}\tau_1} - t_2 e^{i\omega_{ij}(\tau_1+\tau_2)} \dots) \quad (3.4)$$

Here T_{cycle} is the total time of one cycle of the pulse sequence. Now for a chain of n ions, and Stark shift pattern ω_i , we need to choose $\{t_k, \tau_k\}$ such that H_{avg} given in eqn.3.3 would simulate the target Hamiltonian at the end of each cycle.

3.4 Stark shift pattern to simulate 2D lattices

The problem of simulating a graph of interactions inherently divide the pairs of ions into two categories. The pairs which have non zero coupling strength in the desired graph are classified into **Bond** class and other pairs to **Nobond** class. For example to simulate the 2x2 lattice shown in Fig. 3.7,

$$\begin{aligned} \text{Bond class} &= \{(1, 2), (2, 3), (3, 4), (1, 4)\} \\ \text{NoBond class} &= \{(1, 3), (2, 4)\} \end{aligned}$$

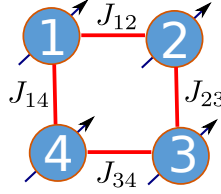


Figure 3.7: (2x2) geometry of 4 ions

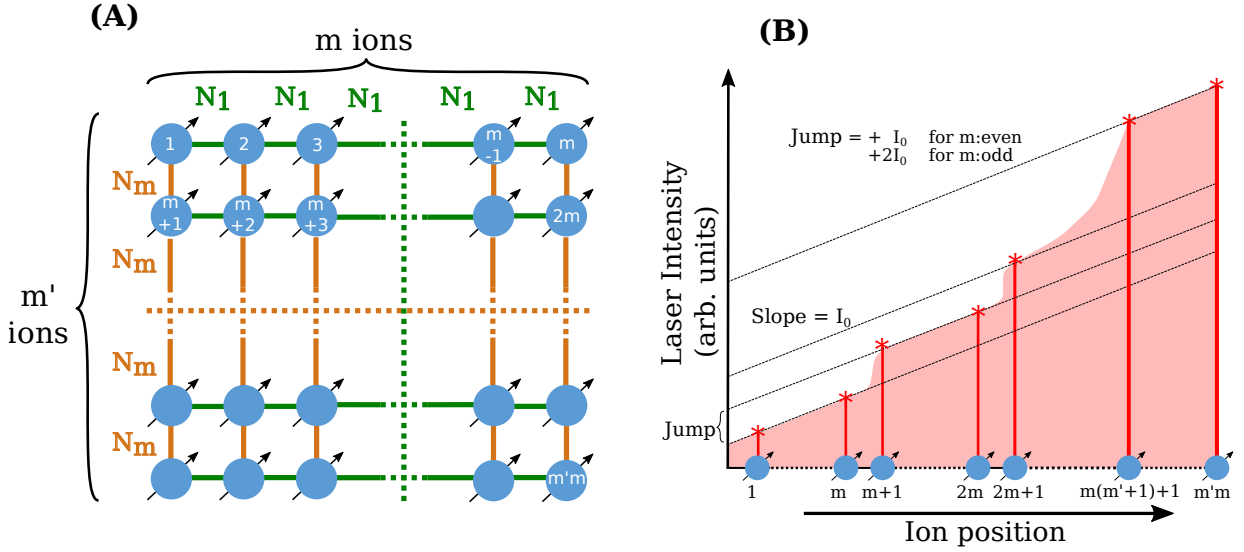


Figure 3.8: Stark gradient scheme to simulate $m \times m'$ 2D lattice

As we can see from eqn. 3.3, for a given pulse sequence $\{t_k, \tau_k\}$ which is global to all ions in a chain, J''_{ij} depends on ω_{ij} . This implies that ω_{ij} should be chosen such that the pulse sequence makes J''_{ij} to zero for **Nobond** class and appropriately scales the **Bond** class. First criteria to be able to do this is to have $\omega_{ij} \neq \omega_{pr}$ for all pairs $(i, j) \in \text{Bond}$ and $(p, r) \in \text{Nobond}$. We can recall from Chapter 2. that these Stark shifts on each ion ω_i are proportional to the laser intensity I_i for a given detuning, thus we need to come up with

a laser intensity pattern I_i to achieve our classification goal. Though there can be many solutions for I_i to satisfy our requirement, the best solution would have properties like

1. Scalable i.e., $I_{max} - I_{min}$ should scale favorably, such as linearly, with the number of ions.
2. Experimentally feasible to implement
3. Requires less reconfiguration of the stark shift pattern (ω_i) for different target geometries

One such intensity pattern to simulate a $m' \times m$ lattice is shown in Fig. 3.8. Let the linear chain of ions be indexed from 1 to n , where $n = m' * m$ for a case of 2D lattice. The numbering scheme for the target 2D lattice is shown in (A) of 3.8, where the index of an ion is counted left to right along a row followed by the next row. For this indexing scheme, the Stark shift laser intensity pattern I_i is shown in (B) of 3.8. This pattern is a linear gradient in intensity with slope I_0 superimposed with additional jumps in intensity after every m ions. This jump in intensity is required to break the bonds of $(l * m, l * m + 1)$ for all $l \in (1, m')$. The jump in intensity depends on the parity of m ,

$$\begin{aligned} \text{Jump} &= +I_0 \text{ for } m:\text{even} \\ &= +2I_0 \text{ for } m:\text{odd} \end{aligned}$$

If the A.C Stark shift corresponding to I_0 is ω_0 , then the set of ω_{ij} tags for Bond class are $\{\omega_0, (m + r + 1)\omega_0\}$ where $r = \text{mod}(m, 2)$ which depends on the parity of m . We will be using this property of this intensity pattern to determine the pulse sequence in the next section.

3.5 Construction of pulse sequence

As the average Hamiltonian from eqn. 3.3 depends on $\{t_k, \tau_k, \omega_i\}$ we need to determine these parameters to match the effective Hamiltonian to the desired one. These set of parameters form the pulse sequence that needs to be implemented during the experiment. We start with the Hamiltonian in eqn. 3.1, where $J_{ij} = \frac{J_0}{|i-j|^\alpha}$ and choose of $\alpha > 0$ (for example 0.2). For this choice α and labelling scheme described in the previous section, the coupling strength $J_{i,i+1} = J_{i,m+i} * m^\alpha$. Thus, our pulse scheme should also rescale $J_{i,i+1}$ to be of able to simulate a 2D lattice with equal interaction strengths between all pairs in Bond class.

To simulate an $m' \times m$ lattice, we start with the Stark shift pattern ω_i described in the previous section. The approach to finding the pulse sequence is to find set values for $\{t_k, \tau_k\}$ such that $J''_{ij}(\{t_k, \tau_k\}) = F(\omega_{ij} * \tau_{tot})$ for all ions i, j , where $\tau_{tot} = \sum_k \tau_k$. The function $F(\omega_{ij} * \tau_{tot})$ is defined as

$$\begin{aligned} J''_{ij}(\{t_k, \tau_k\}) = F(\omega_{ij} * \tau_{tot}) &= 0 && \text{for } (i, j) \in \text{Nobond class} \\ &= \beta/m^\alpha && \text{for } (i, j) \in \text{Bond class and } \omega_{ij} = \omega_0 \\ &= \beta && \text{for } (i, j) \in \text{Bond class and } \omega_{ij} \neq \omega_0 \end{aligned}$$

Here β is the global interaction scaling factor which scales all the interactions of the target Hamiltonian.

The following steps describe the procedure for finding such a pulse sequence

1. Set the value of τ_{tot} such that $\omega_0 * \tau_{tot} = \pi$. With this choice, we can see from eqn. 3.4, $J' = 0$ for all (i, j) where ω_{ij} is an even multiple of ω_0 . The tagging scheme in sec. 3.4 is chosen such that all these $(i, j) \in \text{Nobond class}$. Now we only need to worry about odd multiples of ω_0 .
2. With the choosen value of τ_{tot} we construct the function $F(\omega_{ij} * \tau_{tot})$ for all ion pairs (i, j) such that ω_{ij} is odd multiples of ω_0 .
3. Now, we fit this constructed $F(\phi = \omega_{ij} * \tau_{tot})$ to a Fourier series function $G(\phi) = \sum_{l=0}^{l'} a_l * \cos(iW\phi)$ by optimizing the real valued parameters $\{l', a_l, W\}$. We use these optimized values to find the pulse sequence. Here we have an additional constraint of $\sum_{l=0}^{l'} |a_l| = 1$. To facilitate this constraint while optimizing for the parameters $\{l', a_l, W\}$, we need to set the global interaction scaling factor $\beta < 1$. We have numerically found that $\beta = 0.7$ provides an efficient solutions upto $N = 100$ ions.

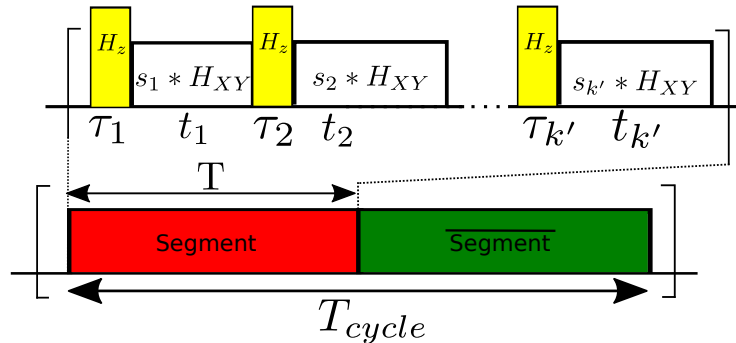


Figure 3.9: A single cycle of the pulse sequence

4. Figure 3.9 shows the structure of a single cycle of the target pulse sequence. It is divided into two segments. The first segment has a sequence of $k' = 2l' + 1$ alternating $\{H_z, s_k * H_{XY}\}$ pulses with times $\{\tau_k, t_k\}$ respectively and $s_k = \pm 1$. The second segment is exactly the same as the first with the signs of H_{XY} inverted, i.e., sequence of alternating $\{H_z, -s_k * H_{XY}\}$ pulses. We use T_{cycle} to denote the total time of each cycle, where as $T = T_{cycle}/2$ denotes the total time of each segment.

For the average Hamiltonian approximation to work as described in sec.3.3, the pulse sequence should satisfy the condition $J_0 * T_{cycle} \ll 1$. Thus for a given initial J_0 , we choose the total time of the pulse sequence as $T_{cycle} = 2\pi \times 0.1/J_0$.

The values of $\{\tau_k, t_k, s_k\}$ depend on our fit parameters $\{l', a_l, W\}$ as follows

$$\begin{aligned}
t_k &= T|a_k/2| && \text{for } k = (1, 2, \dots, l') \\
&= t_{k-l'} && \text{for } k = (l' + 1, \dots, 2l') \\
&= T|a_0| && \text{for } k = 2l' + 1 \\
\\
\tau_k &= \tau_{tot} * W && \text{for } k \neq (l' + 1) \\
&= \tau_{tot} - (l' - 1)\tau_1 && \text{for } k = l' + 1 \\
\\
s_k &= sign(a_k) && \text{for } k = (1, 2, \dots, l') \\
&= -s_{k-l'} && \text{for } k = (l' + 1, \dots, 2l') \\
&= -sign(a_0) && \text{for } k = 2l' + 1
\end{aligned}$$

3.6 Analysis and Results for 6 ions

In this section, I will be illustrating the protocol I have described in the above sections for the case of 6 ions to simulate a (3x2) 2D lattice. We start with a chain of 6 ions interacting with a fully connected flip-flop type interaction described in eqn. 3.1. Here we choose $\alpha = 0.2$ and $J_0 = 2\pi \times 1\text{kHz}$. The Fig. 3.10 illustrates the goal of this simulation. As described before the nodes of this graph are ions and the red, green edges between nodes represent interactions in bond and nobond classes respectively. The protocol suppresses the green edges and rescales red edges to achieve our desired graph.

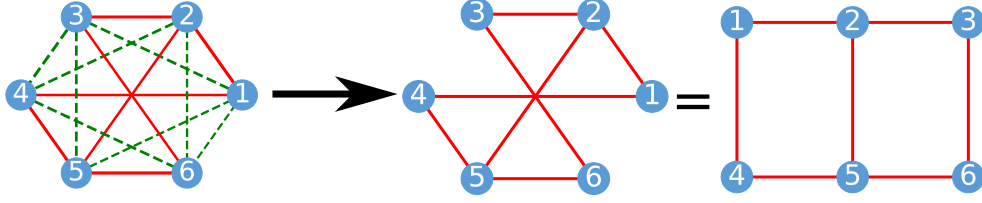


Figure 3.10: Transformation of 6 ion fully connected system to a 3x2 square lattice

The first step in simulating the 2D lattice is to find the Stark intensity pattern described in sec. 3.4. The desired intensity pattern is shown in fig. 3.11, which is a linear gradient of intensity with slope= I_0 , superimposed with a jump($2I_0$) in intensity after 3 ions. The corresponding Stark shift produced from intensity I_0 is ω_0 . For this simulation, we choose $\omega_0 = 2\pi * 500$ kHz.

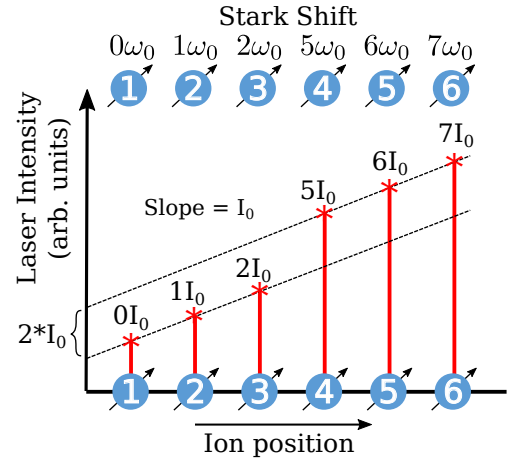


Figure 3.11: Stark gradient for 6 ions

Once the desired Stark shift pattern is determined, the next step is to find the values of $\{\tau_k, t_k\}$ which form the pulse sequence to simulate the lattice. Following the steps 1 and 2 in Sec. 3.5, a function $F(\phi)$ is constructed and fitted with a Fourier series $G(\phi) = \sum_{l=0}^l a_l * \cos(iW\phi)$. We choose the global interaction scaling factor $\beta = 0.7$ to facilitate this fit. This fit is shown in fig. 3.12 and the fit parameters are tabulated.

in states $|\uparrow\downarrow\downarrow\downarrow\downarrow\downarrow\rangle$ and $|\downarrow\uparrow\downarrow\downarrow\downarrow\downarrow\rangle$ is plotted (red trace: Engineered evolution) as a function of time (scaled with J_0) in the figure below (fig. 3.14). Along with this, the evolution of flip-flop Hamiltonian with J_{ij} of target (3x2) square lattice is also plotted (green trace: Target evolution) for comparison. As it can be seen that these evolution plots match with a good agreement for a long time.

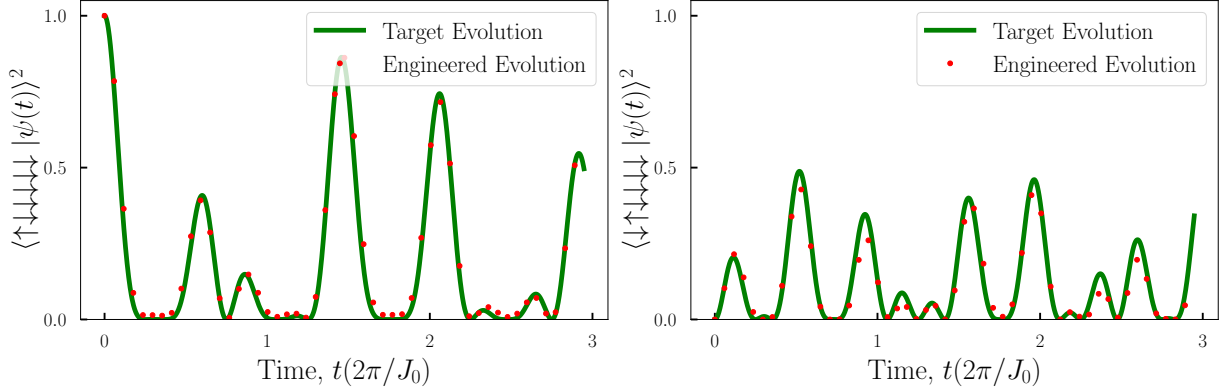


Figure 3.14: Time evolution plots for the case of 6 ions

Even though the evolution plots have a good match, we need to estimate how well we are able to simulate the target interaction graph. To estimate the simulated J_{ij} , the time evolution is done separately for every pair of ions (i, j) by setting $J_{pr} = 0$ for all $(p, r) \neq (i, j)$. The probability $P(|\uparrow\downarrow\rangle)$ for every such evolution is plotted in fig. 3.15

These probabilities are then fit with a cosine function to find the interaction strength J_{ij} which is the angular frequency of the fit. The J_{ij} matrices from such fit are plotted in the fig. 3.16. For comparison, J_{ij} matrices for target (3x2) square lattice and 1D fully connected lattice with $\alpha = 0.2$ are also shown. There is a good match between J_{ij} matrices of the square lattice and engineered lattice with RMS error $< 0.1\%$. Here RMS error is defined as

$$\frac{\sqrt{\sum_{ij} (J_{ij}^E - J_{ij}^T)^2}}{\sum_{ij} |J_{ij}^T|}$$

Where J_{ij}^E, J_{ij}^T denote the couplings in the engineered lattice and ideal target lattice respectively.

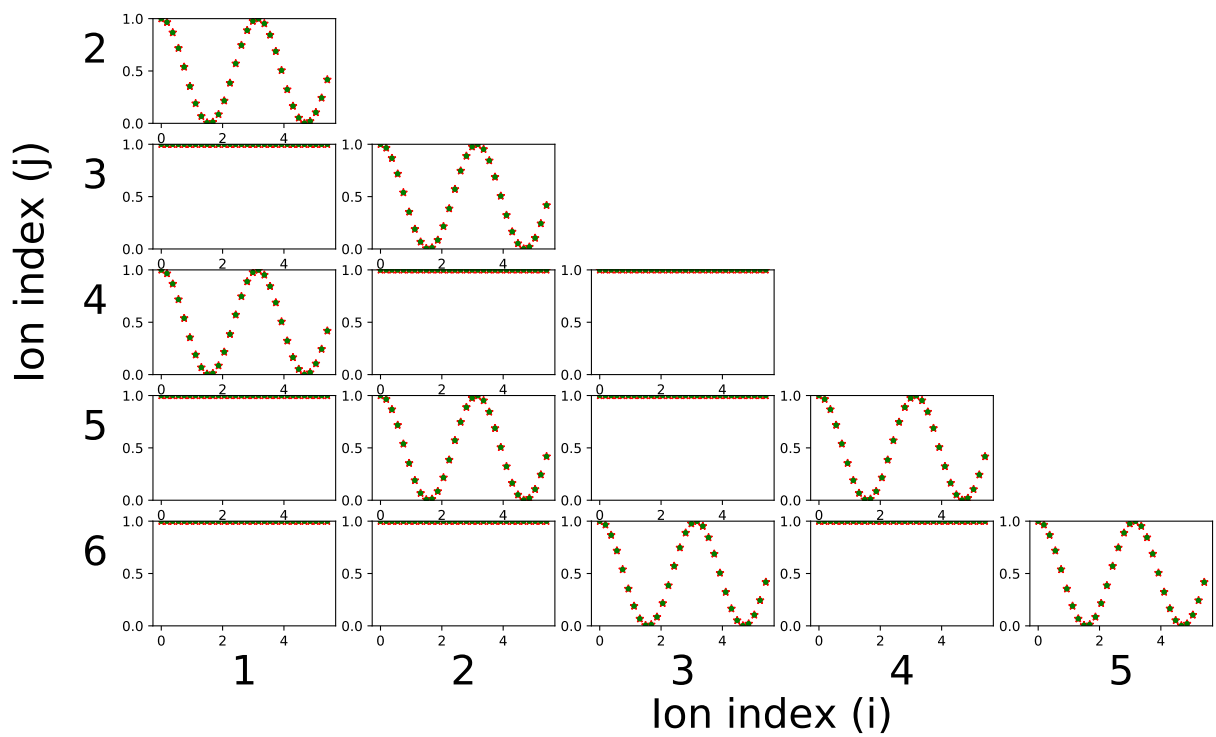


Figure 3.15: 6 ions pairwise time evolution plots

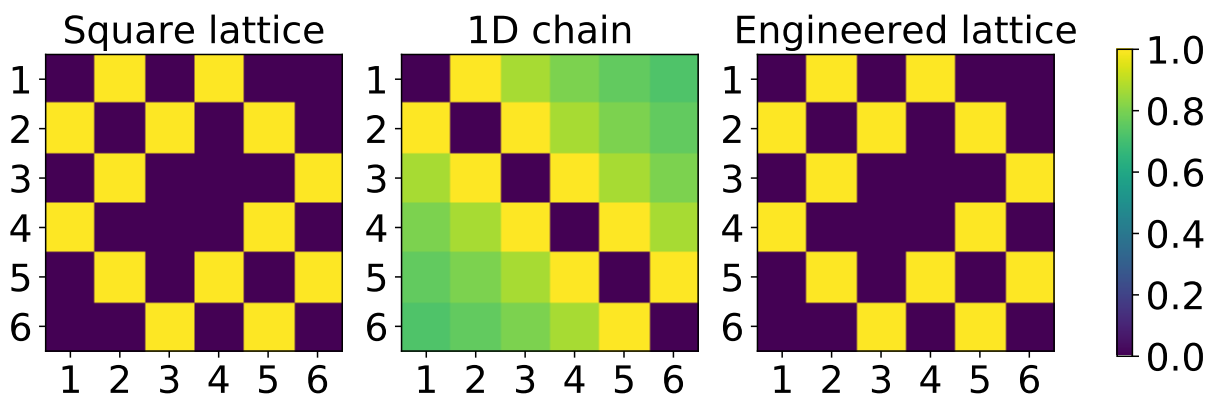


Figure 3.16: Hamiltonian estimation for the case of 6 ions

3.6.1 Simulation with experimental parameters

The above results of simulation start with an assumption that we can simulate a perfect flip-flop Hamiltonian with $J_{ij} = \pm J_0/|i - j|^\alpha$. Deviations from these assumptions during an experiment might lead to errors in the final result. To get a better estimate for how well we can implement this protocol in an actual experimental setup, we perform the simulation with the following experimental parameters. Consider a chain of 6 $^{171}\text{Yb}^+$ ions trapped in a Paul trap with axial and radial trap frequencies as $\omega_X = 2\pi \times 5$ MHz and $\omega_Z = 2\pi \times 1.7$ MHz. The flip-flop Hamiltonian can be simulated from Mølmer-Sørensen scheme by adding an additional transverse magnetic field as described in Chapter 2. For H_{XX} with positive J_{ij} and $\alpha = 0.2$, we use Raman lasers with global Mølmer-Sørensen configuration with detuning $\mu = 2\pi \times 5.055$ MHz with sideband rabi frequency $\eta\Omega = 2\pi \times 18$ kHz. Whereas for the case of negative J_{ij} we use 2 global Mølmer-Sørensen beams with detunings $\mu_1 = 2\pi \times 4.955$ MHz, $\mu_2 = 2\pi \times 4.689$ MHz with sideband rabi frequencies $\eta\Omega_1 = 2\pi \times 15$ kHz and $\eta\Omega_2 = 2\pi \times 4.1$ kHz respectively. Along with these an additional laser which creates a global Stark shift of $\omega = 2\pi \times 10$ kHz is added to transform the H_{XX} to H_{XY} . These parameters create J_{ij} with $\alpha \approx 0.2$ and $J_0 \approx 2\pi \times 520$ Hz. To create H_z we use a laser with site dependent intensity pattern similar to Fig. 3.11 with $\omega_0 = 2\pi \times 500$ kHz. Using these parameters and the pulse sequence determined previously, J_{ij} is estimated for the engineered lattice shown in Fig. 3.17. This result matches with the J_{ij} of the target square lattice with an RMS error $< 2\%$.

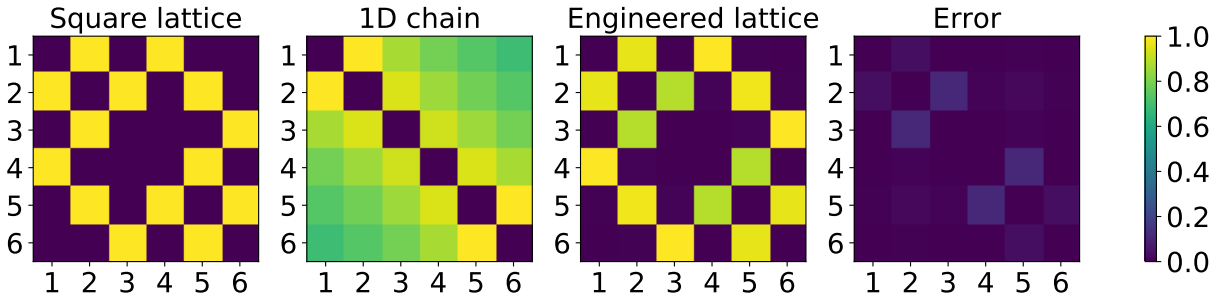


Figure 3.17: Hamiltonian estimation with experimental parameters for 6 ions

3.7 Results for 9,16 ions

In the previous section, we saw that there is a good match of engineered lattice to that of the target lattice for a case of (3x2) 2D lattice from 6 ions. This protocol is scalable to a large number of ions. In this section, some of the results to simulate (3x3) lattice with 9 ions and (4x4) lattice with 16 ions are summarized.

Fig. 3.18 and Fig. 3.20 show the laser intensity pattern to create the site dependent Stark shift for the case of (3x3) lattice and (4x4) lattice respectively. These are patterns with a linear gradient in intensities superimposed with jumps $2I_0$ for 9 ions and I_0 in case of 16 ions. For these simulations similar to above cases we consider $\alpha = 0.2$, $J_0 = 2\pi \times 1$ kHz, $\omega = 2\pi \times 1$ MHz. These simulations are done with an assumption of a perfect flip-flop interaction. Following the steps in sec. 3.5, Fourier fit parameters are found for both the cases and tabulated in Tab. 3.3, Tab. 3.4. Using these pulse sequences desired (4x4) and (3x3) lattice are engineered from fully connected interactions as shown in Fig. 3.19 and Fig. 3.21. These match with target square lattices with RMS error $< 0.1\%$.

Simulating (3x3) lattice using 9 ions

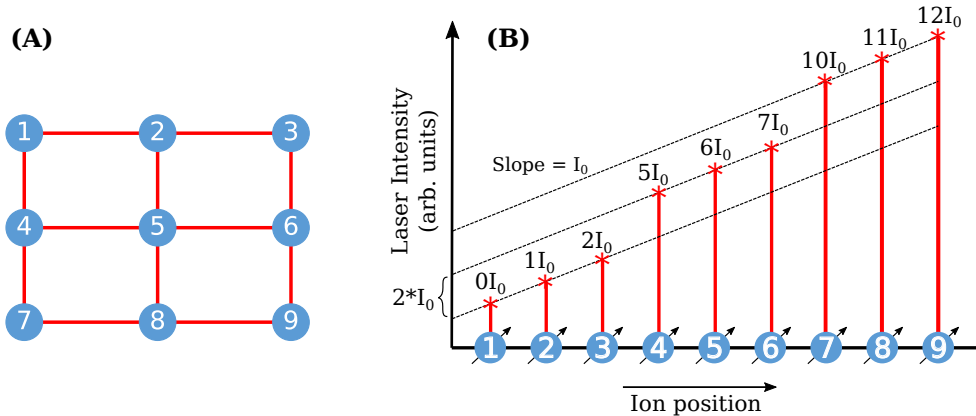


Figure 3.18: Stark gradient pattern for 9 ions

Table 3.3: Fourier series fit parameters for 9 ions

W	a_0	a_1	a_2	a_3	a_4
0.1	0.241	0.204	-0.094	0.126	0.334

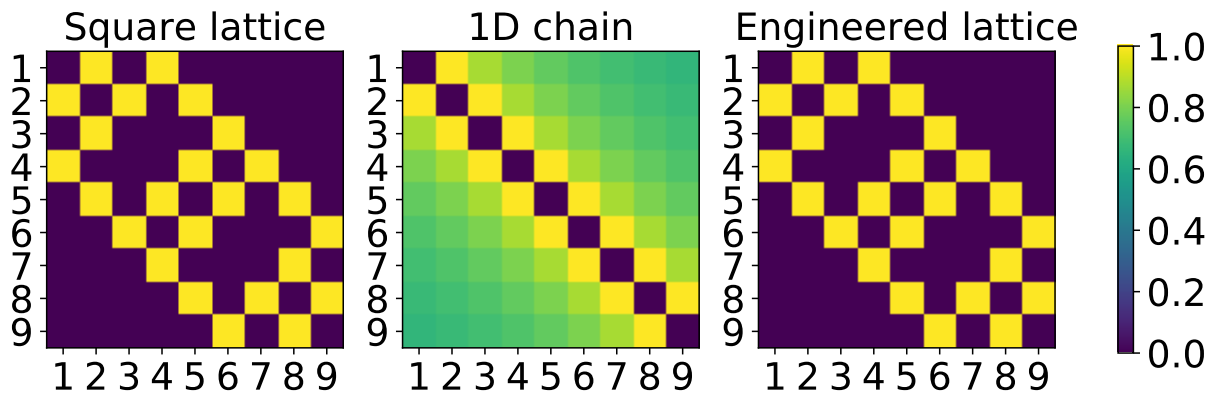


Figure 3.19: Hamiltonian estimation for the case of 9 ions

Simulating (4x4) lattice using 16 ions

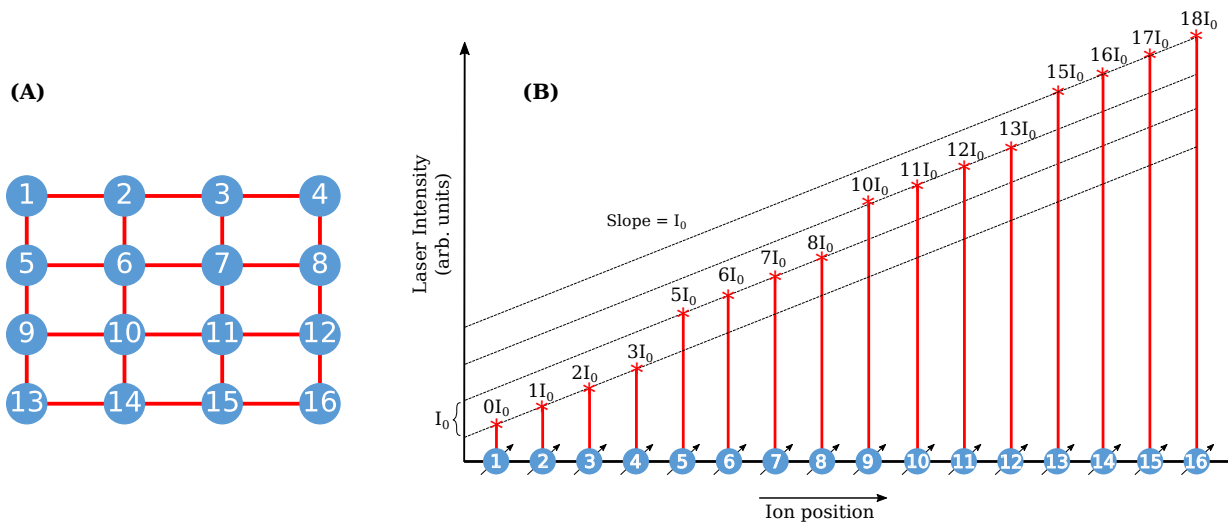


Figure 3.20: Stark gradient for 16 ions

Table 3.4: Fourier series fit parameters for 16 ions

W	a_0	a_1	a_2	a_3	a_4	a_5
0.083	0.204	0.231	-0.048	-0.039	0.204	0.270

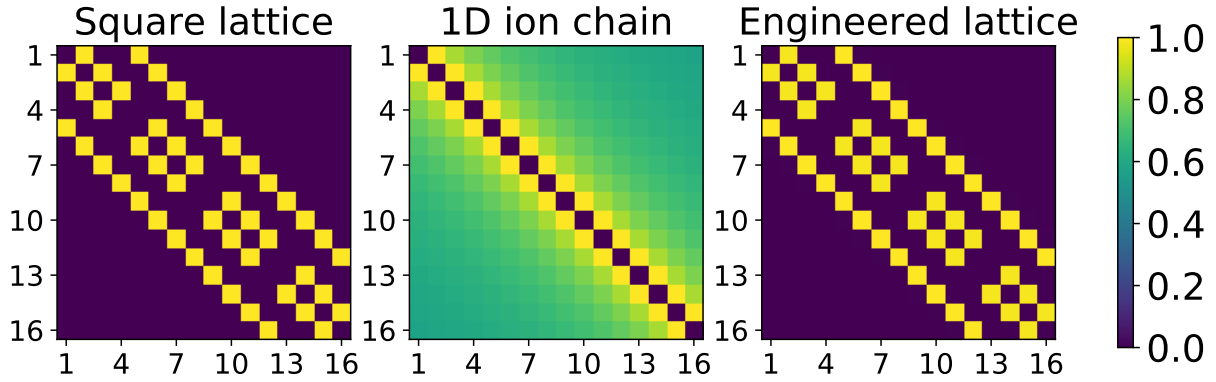


Figure 3.21: Hamiltonian estimation for the case of 16 ions

3.8 Scaling with the number of ions

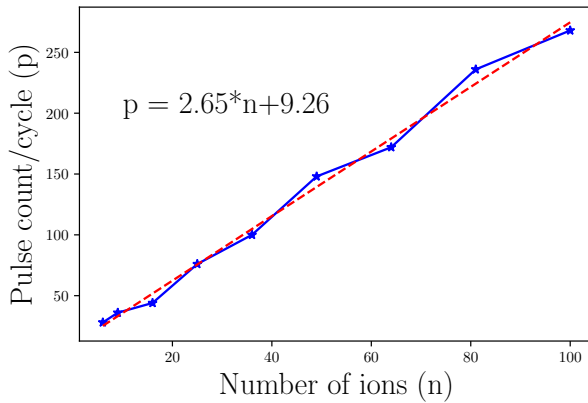


Figure 3.22: Scaling of number of pulses

Previous sections illustrate that the protocol works until the case of 16 ions to simulate (4x4) lattice. One of the important features to look for any simulation is the scaling of resources with the system size. To estimate scaling efficiency for this hybrid simulation, we calculate the number of pulses that are needed to simulate an (mxm) square lattice as a function of the number of ions (shown in Fig. 3.22). We can see that the number of pulses/cycle increases linearly with the number of ions.

3.9 Extension to 3D lattices

More interesting phenomenon can be studied in a system of ions connected in geometries of higher dimensions. This hybrid quantum simulation protocol can also be extended to higher dimensions (3D). Fig. 3.23 illustrates that the transformation of a chain of 8 ions

that are fully connected with a flip-flop interaction with $\alpha \approx 0$ to $(2 \times 2 \times 2)$ 3D lattice. Fig. 3.24 shows the J_{ij} estimation for this engineered lattice which shows a good match with the target lattice.

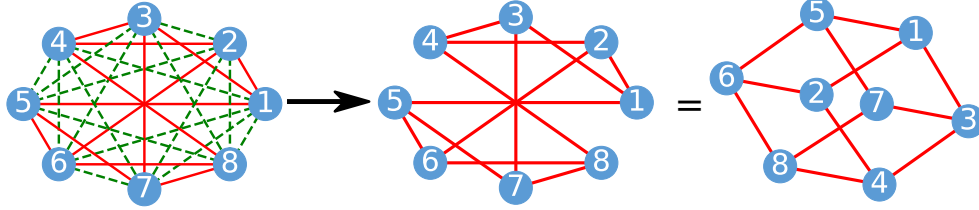


Figure 3.23: Transformation of a fully connected 8 ion chain to a $(2 \times 2 \times 2)$ 3D lattice

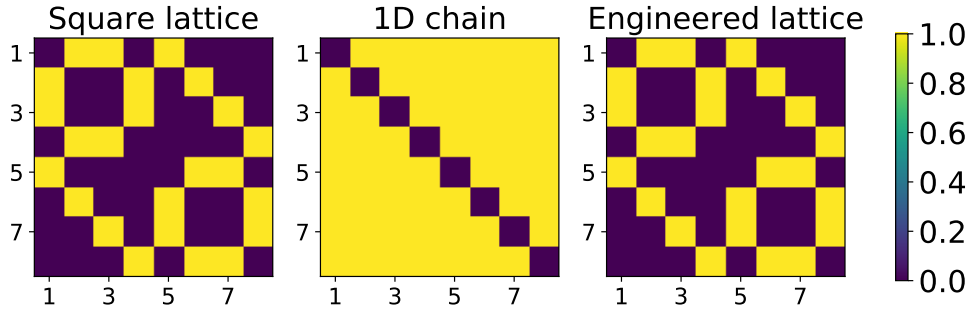


Figure 3.24: Hamiltonian estimation for the case of 8 ions

3.10 Discussion

In Sec. 3.6,3.7, we saw the results of hybrid quantum simulation protocol for the case of 6, 9, 16 ions. These results have a good agreement with the target geometry with RMS error of $< 0.1\%$ (considering only digital part of simulation). In the case of 6 ions, we saw that the RMS error of $< 2\%$ is obtained if we consider the errors from the analog part of this implementation. This protocol scales linearly with the number of pulses (Sec. 3.8) and the Stark intensity gradient increases almost linearly which makes it feasible for experimental implementations with large number of ions, not requiring high gradients in intensities. Thus can be used to study rich physics phenomenon in 2D lattices with a large number of ions, given that $J_0 * T_{cycle} \ll 1$. This approach of average Hamiltonian theory can also be extended to higher geometries like 3D lattices (Sec. 3.9) but scaling of resources for such cases is yet to be studied.

Chapter 4

Laser frequency stabilization

In this chapter, I will be discussing the setup and some results about the frequency locking schemes that stabilize lasers in the context of our lab. As discussed in Chapter 1, a scheme to frequency stabilize lasers against drifts due to various ambient fluctuations like temperature and pressure is required to address various atomic transitions that manipulate the trapped ions.

Any locking scheme that stabilizes an instrument from drifts can be divided into 3 functional blocks

1. **Measurement:** A system which can extract the relevant information from the instrument which will then be used to quantify the drift. For example, this can be a system to measure the frequency of a laser.
2. **Reference:** A reference system/signal which is relatively stable than the target instrument. This will be used to compare the information from the measurement to find the amount of drift.
3. **Feedback:** Once the amount of drift is quantified, this is a system which sends a feedback signal to the target instrument to correct the drift.

The task of stabilizing the laser frequency at the desired value becomes readily feasible if there exists an easily accessible atomic transition near the target frequency. The laser light can then be sent to an atomic source and the attenuation of its intensity at the atomic resonance can be used to lock the frequency. However, a convenient atomic resonance does not exist for all frequencies of relevance. Here we present two alternative schemes for

locking the lasers that will be used in quantum simulation experiments using $^{171}\text{Yb}^+$ ions. These schemes do not rely on an atom source for measurement thus can be used to stabilize lasers from broad wavelength range. For these locking schemes, we try to stabilize DL Pro diode lasers from Toptica with wavelengths 369nm, 399nm, 935nm, Vescent DBR laser of wavelength 760 nm for Yb and 493, 650nm lasers for Ba. These lasers have a reported linewidth of ≈ 100 kHz. These implementations of frequency locks are targeted only to compensate for the drifts and not to decrease the inherent linewidths of the lasers.

4.1 Wavemeter based frequency lock

In this implementation of the frequency lock, the measurement of laser frequency is done using a commercial wavemeter WS-7 from High Finnesse [12]. This wavemeter is based on a Fizeau interferometer. The wavelength/frequency is measured by comparing the interferogram of the input laser beam to a stored calibrated interferogram. This measurement is robust and stable compared to other wavemeters based on Michelson interferometer since it doesn't have any moving parts.

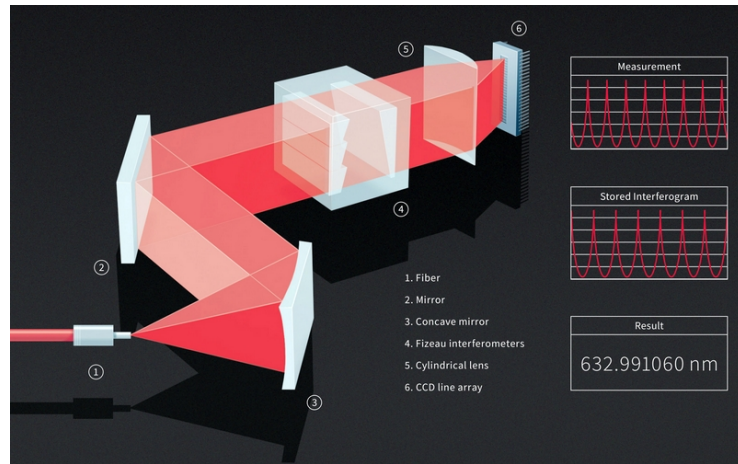


Figure 4.1: Working of a wavemeter [12]

This particular wavemeter can make measurements in a broad range of 330nm - 1100nm, with a reported accuracy of 60 MHz and a precision of 10 MHz. These measurements are made at a sampling rate of 500 Hz. It has an additional attachment of an optical switch, which can be used to measure the wavelengths of 8 different laser beams simultaneously. Though this would result in dividing the sampling rate among the various measurements.

This wavemeter also contains an inbuilt pressure and temperature sensors which can be used to understand the correlations of change in ambient pressure and temperatures with the change in laser frequency. Fig. 4.2 shows the drift in laser frequency(unlocked 935nm laser), pressure, temperature measured using this wavemeter as a function of time. We can clearly see the correlation between the laser frequency and ambient pressure in this graph. The drift in measurement can be the result of both the drift in laser frequency and the wavemeter interferometers.

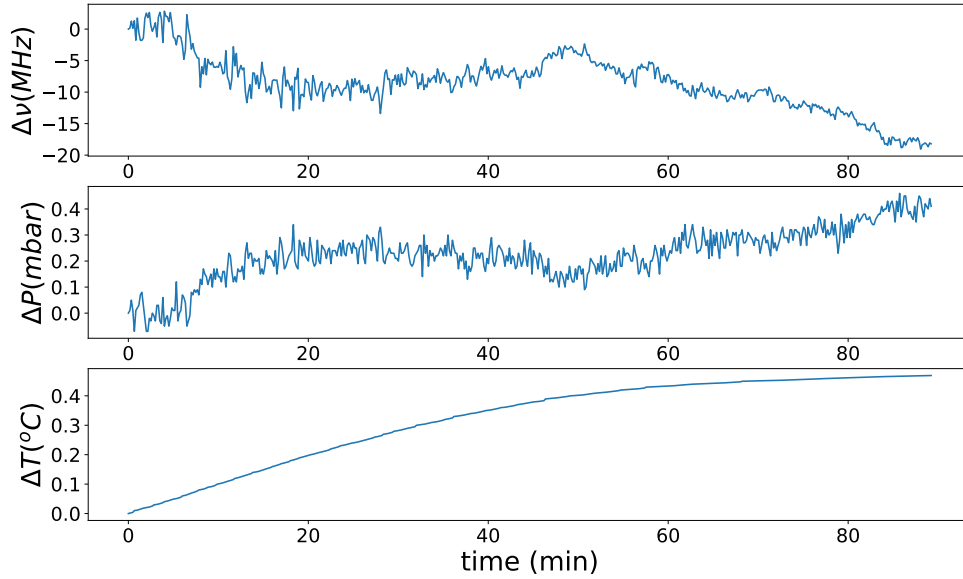


Figure 4.2: Drift of frequency due to ambient fluctuations

Using the above mentioned wavemeter and optical switch, we implement a frequency lock, the scheme of which is shown in Fig. 4.3. Laser beams from multiple lasers are sent to the optical switch using multiple single mode FC/APC to FC/PC optical fibers. Another multimode fiber is connected from the common port of the optical switch to the wavemeter. This wavemeter is also pre-calibrated to a 780nm laser that is locked to a Rubidium reference. The acquisition of interferogram and control of the optical switch is done by a software (supports only Microsoft Windows operating system) provided by the manufacturer. After the acquisition, the software calculates wavelength from the interferograms and display it on screen. This control software is a single threaded program which is not efficiently written, so other programs running in the same CPU affect the sampling rate of the measurement. The sampling rate even decreases when the GUI of the software if maximized compared to that of the minimized. To avoid these issues of sampling

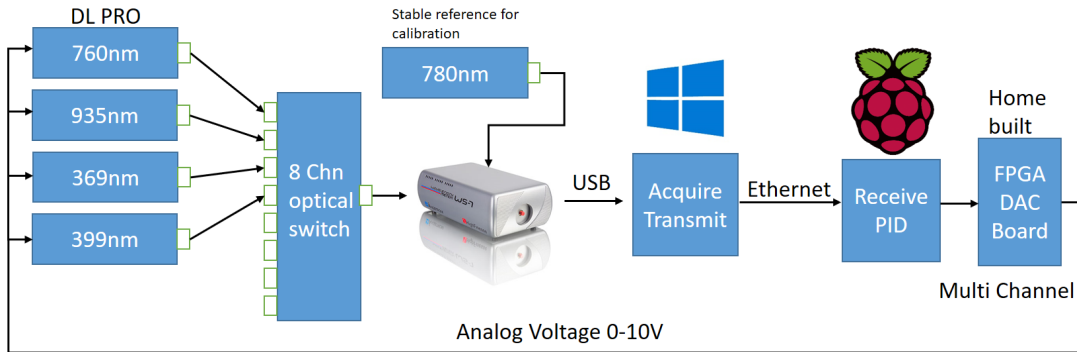


Figure 4.3: Wavemeter lock scheme

rates, a dedicated computer based on Intel NUC [13] is used to perform the measurements. This computer has a small form factor of 4”x4”x2” and is equipped with an i3 processor, 8GB RAM, 256GB SSD. It also runs a python server which grabs the information about the wavelength (using an API provided by the manufacturer) and transmits it over the Ethernet. A client python program running in a computer based on a Raspberry PI 3B+, receives the wavelength information from the server and then calculates the error from the set-point wavelength. This client then feedbacks the lasers by sending a voltage to the piezo-actuator of lasers which is a function of error calculated.

The feedback voltage is generated using home built Digital to Analog Converter (DAC) boards based on DAC7744[14] that are controlled using an FPGA based on a Xilinx Spartan 6 [15]. This home built FPGA DAC system has a master FPGA board and daughter DAC boards, each of which has a 4 channel DAC7744 DAC. Each daughter board has 4 analog outputs with range $\pm 10V$, sampling rates of 100ksps. Additionally, each board has a 6bit DIP switch which sets the address of the board. This address is used to target daughter board from the master board.

To check the response of the feedback system on the change of laser frequency, the piezo of the laser is scanned at a frequency of 10 Hz which in turn changes the frequency of the laser. The scanning voltage can be seen as the yellow trace in Fig. 4.4. The wavelength is measured by the wavemeter and a voltage signal proportional to the error is generated which can be seen as the blue trace in Fig. 4.4. We can see that our feedback system can follow the changes with a lag which is inherent from delay in wavemeter measurement.

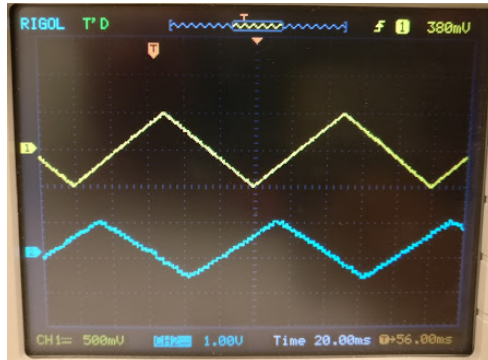


Figure 4.4: Response of the feedback circuit with the scanning of laser piezo

Locking results

Using this locking scheme mentioned above PID parameters are found using ZieglerNichols method [16] for DL Pro optica laser with wavelength 935nm. These PID parameters are then used to calculate the feedback voltage as a function error signal. Using the PID parameters obtained for 935nm laser, the wavemeter lock has been implemented to lock 935nm laser from the drifts. The comparison of drift of frequency in situations of locked vs unlocked is shown in Fig. 4.5. As we can see that the locked laser doesn't drift for long periods of time. This locking scheme is limited by the precision and accuracy of the wavemeter.

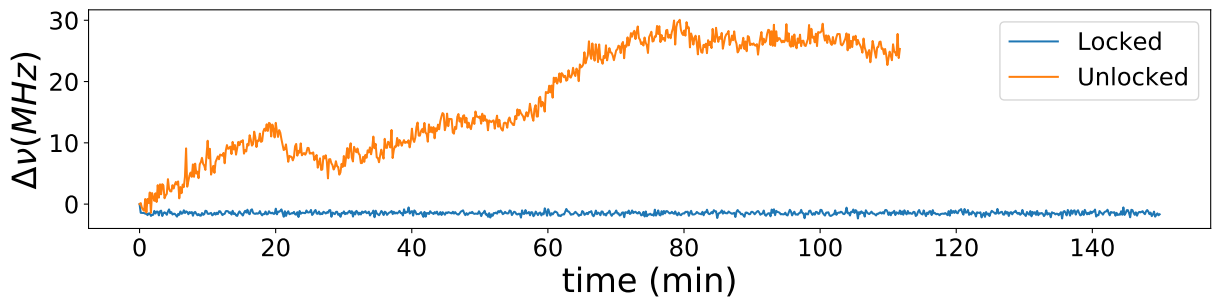


Figure 4.5: Locked laser vs unlocked laser

4.2 Cavity based frequency lock

Another solution for frequency locking lasers is using a Fabry Perot (FP) cavity to measure the drifts in laser frequencies. The goal of this thesis is to build a cavity that is used to monitor the laser frequency and can be further used to lock the lasers. In this chapter, I will discuss the construction and optical setup for the cavity followed by a proposal for a layout of the cavity based frequency lock.

A Fabry Perot (FP) cavity is an optical resonator that transmits a laser beam coupled into it only when the length of the cavity is an integral multiple of the wavelength. Thus for a given cavity length, the transmitted signal is a function of frequency. The cavity can thus be used for measuring absolute frequencies if the cavity length is accurately known. But now the stability of the measurement would depend on how stable the length of the cavity is against drifts in ambient temperature and pressure fluctuations. Thus the cavity cannot be practically used to make an absolute measurement of frequency. A workaround for this problem is to use the cavity to make a relative measurement of frequencies between two laser beams. Given that one of the lasers is stabilized (for example to an atomic reference) the drift of the relative measurement quantifies the drift of the second laser. This relative measurement is not very sensitive to the length of the cavity, thus can be more stable.

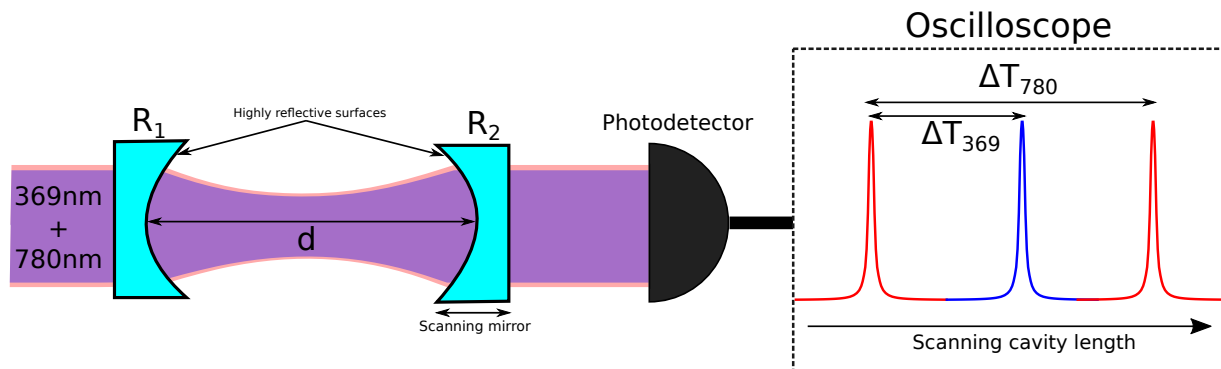


Figure 4.6: Cavity lock working. Light from 369nm and 780nm lasers are coupled into a cavity with a scanning mirror. R1, R2 are the radii of curvature for the cavity mirrors. The transmitted light detected by a photodetector and the signal is displayed on an oscilloscope.

In this particular implementation, a DL Pro laser from toptica at 780nm is used as a stable reference for the relative measurement. This laser is locked to an atomic transition of Rubidium. To lock a frequency of a laser, say a 369nm laser, both 369nm and 780nm laser beams are coupled into the cavity which is continuously scanning one of its mirrors to

change the cavity length. A photodiode after the cavity measures the transmission peaks of both 369nm and 780nm beams as shown in Fig. 4.6 as a function of time. Let ΔT_{780} be the time interval between 2 transmission peaks of 780nm and ΔT_{369} is the interval between one of the transmission peaks of 780nm and a 369nm peak. The feedback scheme tries to keep the ratio of $\Delta T_{369}/\Delta T_{780}$ constant. This scheme is scalable, we can use a single FP cavity to lock multiple lasers of wavelengths 369nm, 399nm, 760nm, 935nm simultaneously. In the following sections, I will discuss the design and construction of a cavity which is designed to perform the above mentioned locking scheme.

4.2.1 Cavity design

The cavity in our implementation is made of two custom concave mirrors of the radius of curvature (R1 and R2) 150mm (procured from Photop technologies inc.). These mirrors have a highly reflective (HR) surface with $R > 99.5\%$ for all the wavelengths of interest. The reflectivity of these mirrors is important since the finesse (Free Spectral Range/Full Width at Half Maximum) of transmission peaks depend on the reflectivity as $\approx 2\pi/\rho$ where ρ is the round trip loss of the light inside the cavity. This leads to a cavity finesse of ≈ 1000 for all the wavelengths. The transmission curve for the HR coating of one of this mirrors is shown in Fig. 4.7.

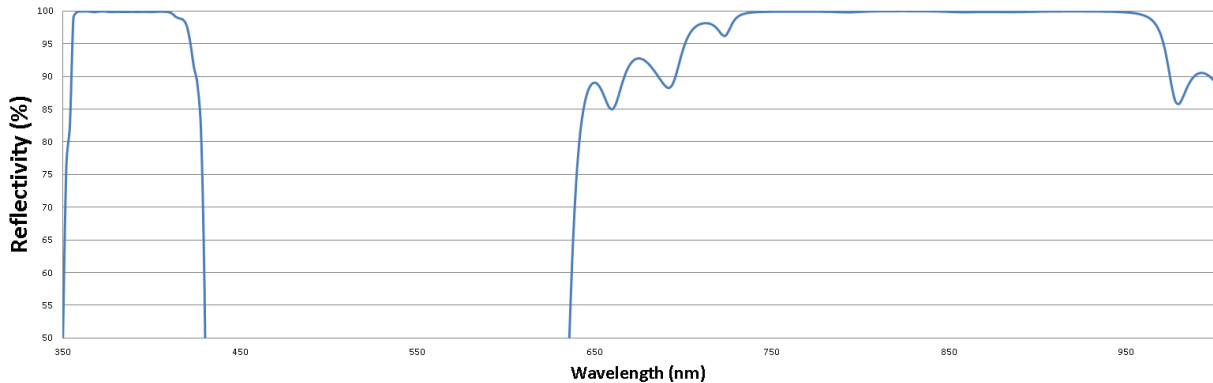


Figure 4.7: Predicted trasmission profile of the HR mirrors

Other than the reflectivity of the cavity mirrors, the parameter that affects the resolution of the measurement is the length of the cavity. The length of the cavity (d) should be such that it meets the cavity stability criteria given by

$$0 \leq g_1 * g_2 \leq 1$$

where

$$g_i = \left(1 - \frac{d}{R_i}\right)$$

For our implementation we chose $d = 100\text{mm}$ which results in $g_1 * g_2 = 0.11$, satisfying the stability criteria of an FP cavity. The resulting cavity would have $\text{FSR} \approx 1.5\text{ GHz}$ and $\text{FWHM} \approx 1.5\text{ MHz}$ for $\text{finesse} = 1000$. This means that the cavity can resolve 2 frequencies that are separated by 1.5 MHz.

4.2.2 Cavity construction

Even though this measurement scheme of frequency doesn't get much affected by cavity length, minimizing the cavity drift is essential to be able always stay in a stable cavity scanning regime. The construction of this cavity is inspired from the design of Fabry Perot cavity presented in John Barry's PhD thesis (Yale University)[17]. The cavity support is made of two materials, Brass and Quartz. The support consists of two end caps made of brass. One of the end caps has a movable part while the other is a fixed part. This configuration facilitates a coarse adjustment in the cavity length. The fixed end also consists of a piezoelectric actuator for fine adjustment. These end caps are attached together with a quartz tube.

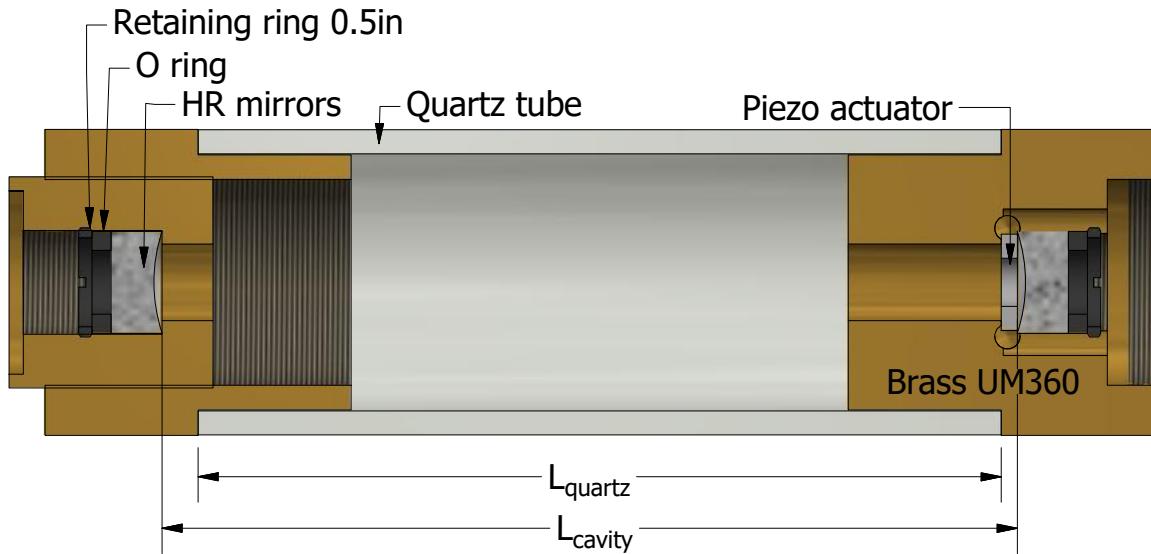


Figure 4.8: Construction of cavity supports

Fig. 4.8 shows the cross section of such a cavity assembled with the HR mirrors. The dimension L_{cavity} is decided to be 100mm as discussed in the previous section. The dimensions of the quartz tube and brass end caps are decided such that they compensate the thermal expansion of each other to minimize the thermal drift to the first order. Thus

$$L_{cavity} = L_{brass} + L_{quartz} + L_{piezo}$$

and

$$\Delta L_{cavity} = \alpha_{brass}L_{brass} + \alpha_{quartz}L_{quartz} + \alpha_{piezo}L_{piezo}$$

Given L_{piezo} and L_{cavity} the value of L_{quartz} is determined from the above equations for $\Delta L_{cavity} = 0$ and machined to an accuracy of 1/1000th of an inch. This setup should ideally cancel the thermal drift of the cavity to the first order, given the temperature is homogenous across the system.

Another source of error in measurement is fluctuations in the refractive index due to the variation of air pressure inside the cavity and also due to differences in the dispersion of various wavelengths in air. To minimize this error the cavity is enclosed in a vacuum assembly as shown in Fig. 4.9. This chamber is made of a KF50-KF40 Tee adapter. Two KF50 ports are used to transmit the light, while the KF40 port is used to send the voltage to the piezo and also to evacuate the chamber.

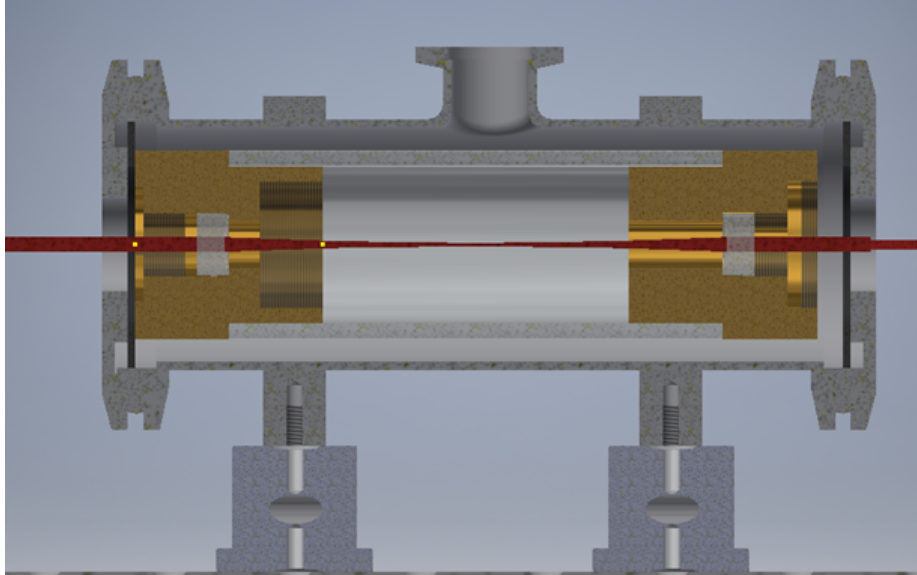


Figure 4.9: Cavity vacuum enclosure

4.2.3 Optical setup and cavity mode matching

To efficiently use this scheme of locking, only the fundamental mode of the cavity should be excited. To do this the input mode of light into the cavity should match the fundamental mode of the optical resonator. The cavity mode parameters can be calculated from the dimensions of the cavity mirrors and the length of the cavity. Due to the symmetry of the cavity setup, the beam waist of the fundamental mode occurs at the center of the cavity. The beam waist inside the cavity is given by

$$w_0 = \sqrt{\frac{z_R \lambda}{\pi}}$$

where

$$z_R = \sqrt{\frac{d}{2} * (R_1 - \frac{d}{2})}$$

z_R is the Rayleigh length of the fundamental mode inside the cavity. As we can see from the expression of beam waist w_0 , it is a function of the wavelength. Thus one has to beam shape all the incident beams separately to match the mode. Other than beam waist the radius of curvature of the wavefront should also be matched at the center of the cavity. Both these parameters are usually grouped together as the complex beam parameter q . The q parameter for the cavity at its center is given by $q = iz_R$. The gaussian beam propagation inside the cavity for the 369nm laser is shown in Fig. 4.10.

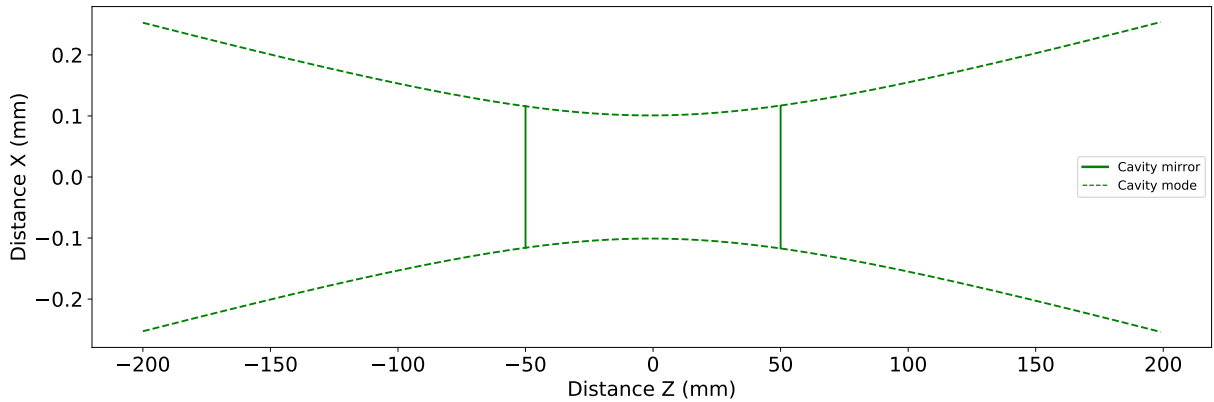


Figure 4.10: Fundamental mode of the cavity at 369nm. The X-axis is the distance along the propagation of light and Y-axis is the distance perpendicular to the direction of light.

To match the mode of laser beam collimated from the fiber coupler a series of lens L1, L2, L3 are used to shape the beam (Fig. 4.13). L1, L2 form a Galilean telescope which

shrinks the beam waists and then a common lens L3 focuses all the beams to the center of the cavity. The values of FC, L1, L2, L3 are optimized based on input beam size and the commercial availability. The match for 369nm laser is shown in Fig. 4.11. As we can see that the pair of lens L1, L2, L3 matches the gaussian beam waist and the curvature of the input laser beam to that of the cavity.

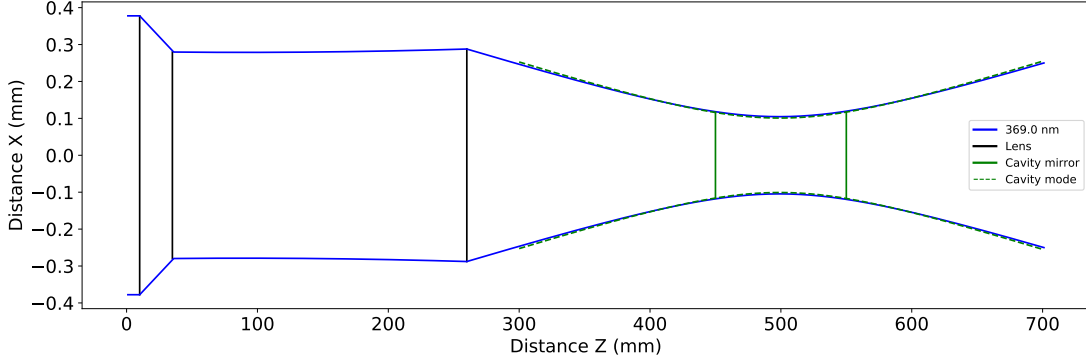


Figure 4.11: Mode matching for the 369nm laser beam. The X-axis is the distance along the propagation of light and Y-axis is the distance perpendicular to the direction of light.

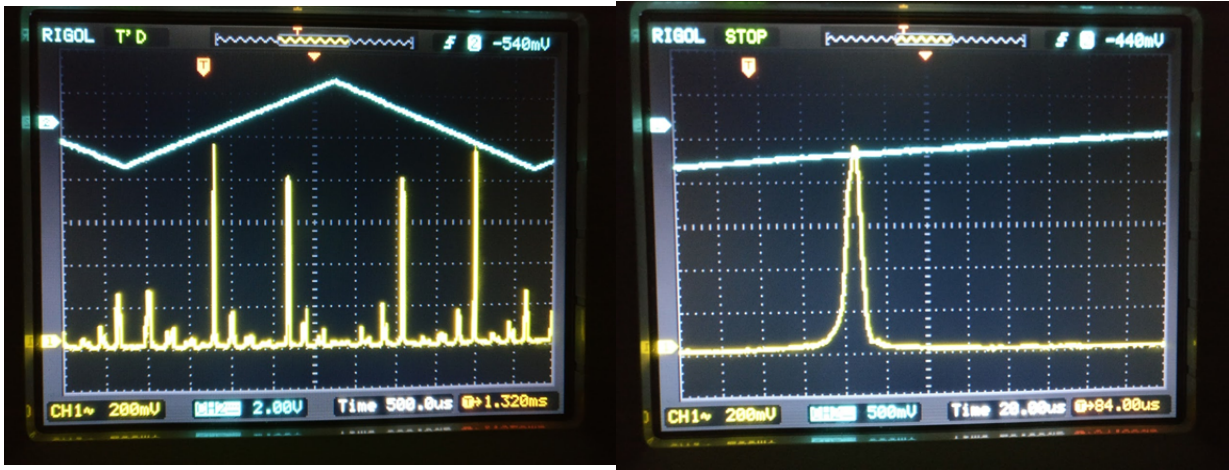
Using an interactive python code I optimized the values FC, L1, L2, L3 and tabulated in the table below

Table 4.1: Cavity mode matching parameters

wavelength(nm)	f_{FC} (mm)	f_1 (mm)	f_2 (mm)	Ld(mm)	f_3
369.0	4.02	150.0	-75.0	75.0	150.0
399.0	4.02	150.0	-75.0	75.0	150.0
760.0	8.00	125.0	-50.0	74.0	150.0
780.0	8.00	125.0	-50.0	74.0	150.0
935.0	8.00	150.0	-50.0	99.0	150.0

4.3 Cavity transmission measurements

Using the construction scheme mentioned in Sec. 4.2.2, I have built the cavity and the finesse of the cavity is measured at 780nm. Fig. 4.12a and 4.12b show the transmission peaks at 780nm. A Lorentzian finesse of ≈ 400 was achieved.



(a)

(b)

Figure 4.12: Cavity transmission

4.4 Optical layout for cavity based frequency lock

In this section, I propose an optical layout for the cavity based frequency lock using the cavity I have described in previous sections. The optical layout of the scheme is shown in Fig. 4.13. Light from various optical fibers is collimated using a fiber collimator followed by beam shaping optics to mode match the cavity. All the lasers beams are then merged using multiple dichroic mirrors and coupled into the cavity. The transmission of multiple such lasers is separated using a system of dichroic mirrors and then detected using photodiodes. An FPGA based PID receives the signal from the photo detectors and feedbacks the lasers to compensate for the drift.

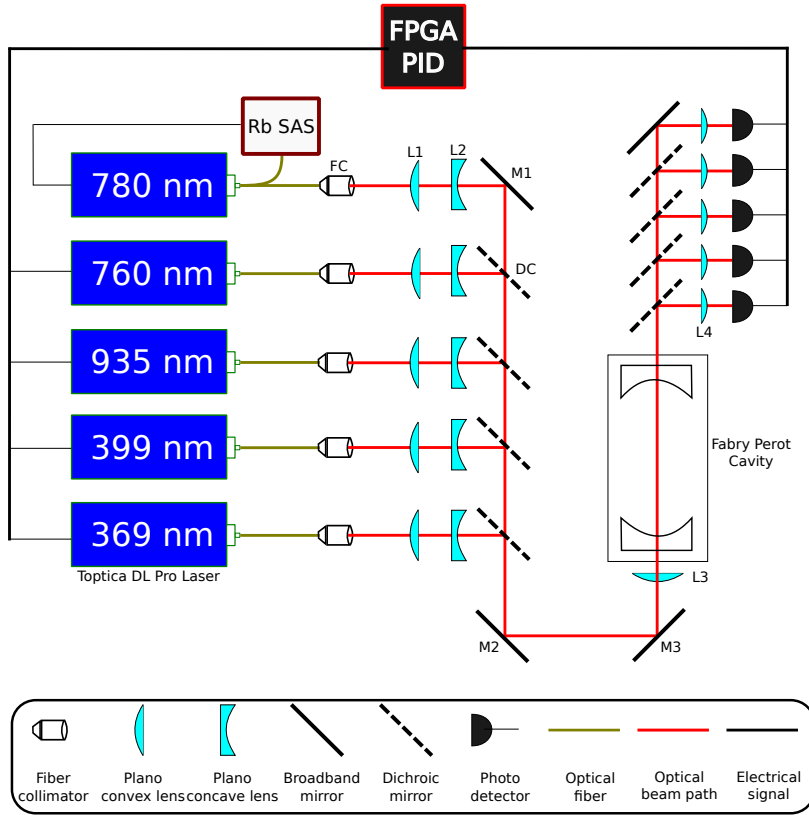


Figure 4.13: Cavity lock optical layout

4.5 Discussion

In the previous sections, I have discussed two schemes of locking the lasers as alternatives to using an atomic source as a reference. These schemes are scalable and don't depend much on the wavelength of operation. Though the first scheme using the wavemeter has advantages of ease and scalability, it is limited by the resolution and sampling time of the instrument. The cavity based lock has more resolution of measurement, but is limited that we cannot make an absolute measurement of the frequency. So we plan to use the combination of both the schemes where the first scheme will be used to make an absolute measurement of the frequency so that we can park the lasers at the known frequency from the literature and then use the cavity based frequency locking scheme to implement a more robust lock.

Chapter 5

Summary and Outlook

In this thesis, I have discussed some theoretical and experimental tools I have developed in the context of our lab for implementing a hybrid (analog-digital) quantum simulator.

5.1 Engineering 2D lattices from 1D chain of ions

Chapter 3 describes the protocol and some theoretical results for simulating 2D lattices from a 1D chain of ions. It can be seen that theoretically, the engineered lattice interaction profile matches to that of the target 2D lattice with error $< 0.1\%$ (only digital part). But, if we consider the analog part of the simulation the error is $< 2\%$ for the case of 6 ions. This error is mainly due to the imperfections in the simulation of $J_{ij} = \pm 1/r^\alpha$ type interaction profiles. The error decreases if the detuning μ is closer to the COM mode but this implies we need to decrease the energy scale of the system since we don't want to excite the phonons. This makes the simulations slower, limiting the number of cycles one can evolve the system for a given coherence time. More work needs to be done to estimate these errors for the case of larger system sizes. The stark pattern as discussed in Sec. 3.4 has a profile of a linear gradient superimposed with jumps. Such patterns can be generated using devices like spatial light modulators, acousto-optic deflectors. More work needs to be done on exploring such solutions to generalize this protocol for simulations of arbitrary higher geometries.

5.2 Laser frequency stabilization

Chapter 4 describes two schemes for locking the frequency of lasers. We can see that the implementation of the locking scheme using the commercial wavemeter is limited by its inherent accuracy of 60 MHz. One of the reasons for this limitation is the drift of measurement apparatus due to ambient pressure and temperature fluctuations. As an improvement, the instrument could be enclosed in a chamber with pressure and temperature control thus decreasing the drift. For the case of the cavity based lock, I have shown the construction and some results of the cavity transmission spectrum. At the time of writing this thesis the locking scheme based on FPGA based electronics is still under construction. This includes a circuit with a series of photodetectors to detect the light from various wavelengths, an oct channel Analog to Digital converter (ADC) board to acquire signals from the photo detectors and send to the FPGA board. This FPGA then feedbacks the lasers using the DAC board discussed in chapter 4. Additionally the coupling into the cavity has to be improved using the mode matching lens discussed in Sec. 4.2.3.

References

- [1] S. Korenblit, D. Kafri, W. C. Campbell, R. Islam, E. E. Edwards, Z.-X. Gong, G.-D. Lin, L. Duan, J. Kim, K. Kim, *et al.*, “Quantum simulation of spin models on an arbitrary lattice with trapped ions,” *New Journal of Physics*, vol. 14, no. 9, p. 095024, 2012.
- [2] K. Mølmer and A. Sørensen, “Multiparticle entanglement of hot trapped ions,” *Physical Review Letters*, vol. 82, no. 9, p. 1835, 1999.
- [3] P. Richerme, Z.-X. Gong, A. Lee, C. Senko, J. Smith, M. Foss-Feig, S. Michalakis, A. V. Gorshkov, and C. Monroe, “Non-local propagation of correlations in quantum systems with long-range interactions,” *Nature*, vol. 511, no. 7508, p. 198, 2014.
- [4] R. P. Feynman, “Simulating physics with computers,” *International journal of theoretical physics*, vol. 21, no. 6-7, pp. 467–488, 1982.
- [5] D. P. DiVincenzo, “The physical implementation of quantum computation,” *Fortschritte der Physik: Progress of Physics*, vol. 48, no. 9-11, pp. 771–783, 2000.
- [6] Y. Wang, M. Um, J. Zhang, S. An, M. Lyu, J.-N. Zhang, L.-M. Duan, D. Yum, and K. Kim, “Single-qubit quantum memory exceeding ten-minute coherence time,” *Nature Photonics*, vol. 11, no. 10, p. 646, 2017.
- [7] D. Hayes, S. T. Flammia, and M. J. Biercuk, “Programmable quantum simulation by dynamic hamiltonian engineering,” *New Journal of Physics*, vol. 16, no. 8, p. 083027, 2014.
- [8] R. Islam, C. Senko, W. Campbell, S. Korenblit, J. Smith, A. Lee, E. Edwards, C.-C. Wang, J. Freericks, and C. Monroe, “Emergence and frustration of magnetism with variable-range interactions in a quantum simulator,” *Science*, vol. 340, no. 6132, pp. 583–587, 2013.

- [9] S. Olmschenk, K. Younge, D. Moehring, D. Matsukevich, P. Maunz, and C. Monroe, “Manipulation and detection of a trapped yb^+ hyperfine qubit,” *Physical Review A*, vol. 76, no. 5, p. 052314, 2007.
- [10] J. Johansson, P. Nation, and F. Nori, “Qutip: An open-source python framework for the dynamics of open quantum systems,” *Computer Physics Communications*, vol. 183, no. 8, pp. 1760–1772, 2012.
- [11] J. Johansson, P. Nation, and F. Nori, “Qutip 2: A python framework for the dynamics of open quantum systems,” *Computer Physics Communications*, vol. 184, no. 4, pp. 1234–1240, 2013.
- [12] HighFinesse, “WS7-60 Wavelength Meter.” <http://www.highfinesse.com/en/wavelengthmeter>.
- [13] Intel, “NUC.” <https://www.intel.com/content/www/us/en/products/boards-kits/nuc.html>.
- [14] Texas Instruments, “Dac7744 16-bit, quad voltage output digital-to-analog converter.” <http://www.ti.com/product/DAC7744>.
- [15] Xilinx, “Spartan-6.” <https://www.xilinx.com/products/silicon-devices/fpga/spartan-6.html>.
- [16] Wikipedia contributors, “Ziegler–Nichols method — Wikipedia, the free encyclopedia,” 2018. https://en.wikipedia.org/wiki/Ziegler%E2%80%93Nichols_method.
- [17] J. Barry, “Laser cooling and slowing of a diatomic molecule,” 2013. <https://demillegroup.yale.edu/sites/default/files/files/John%20Barry%20Thesis%20website%20version.pdf>.

List of Publications

The theory and the numerical results described in Chapter 3 have been summarized in the following preprint

F. Rajabi, **S. Motlakunta**, C.-Y. Shih, N. Kotibhaskar, Q. Quraishi, A. Ajoy, and R. Islam, “Dynamic Hamiltonian engineering of 2D rectangular lattices in a one-dimensional ion chain,” arXiv:1808.06124, (2018).